

# Radial Velocity Monitoring of the Young Star Hubble 4: Disentangling Star-spot Lifetimes from Orbital Motion\*

Adolfo Carvalho 

Christopher M. Johns-Krull 

L. Prato 

And Jay Anderson 

Rice University, Department of Physics and Astronomy, Houston, TX 77005, USA

Lowell Observatory, 1400 Mars Road, Flagstaff, AZ 86001, USA

STSCI, 3700 San Martin Drive, Baltimore, MD 21218, USA

Received 2020 September 23; revised 2021 January 27; accepted 2021 January 31; published 2021 March 24

#### Abstract

We studied the weak-lined T Tauri star Hubble 4, a known long-period binary, and its star-spot phenomena. We used optical radial velocity (RV) data taken over a span of 14 yr (2004–2010, 2017–2019) at the McDonald Observatory 2.7 m Harlan J. Smith Telescope and single epoch imaging from the Hubble Space Telescope (HST)/Wide Field Camera 3 instrument. The observed and apparent RV variations show contributions, respectively, from the binary motion as well as from a large spot group on one of the stars, presumed to be the primary. Fitting and removing the orbital signal from the RVs, we found the lower bound on the lifetime of a previously identified large spot group on the surface of the star to be at least 5.1 yr. An ~5 yr lower limit is a long, but not unprecedented, duration for a single spot group. The later epoch data indicate significant spot evolution has occurred, placing an upper bound on the spot group lifetime at 12 yr. We find that pre-main-sequence evolutionary models for the age of Taurus (~2 Myr), combined with component mass estimates from the literature, permit us to reproduce the HST relative photometry and the binary-induced contribution to the apparent RV variations. The long-lived star spot we find on Hubble 4 has significant implications for dynamo models in young stars, as it adds evidence for long lifetimes of magnetic field topologies. There are also significant implications for young star exoplanet searches, as long-lived coherent RV signals may be spot induced and not the result of planetary motion.

Unified Astronomy Thesaurus concepts: Radial velocity (1332); T Tauri stars (1681); Star spots (1572); Binary stars (154); Pre-main-sequence stars (1290); Stellar activity (1580); Stellar flares (1603); Optical flares (1166)

### 1. Introduction

T Tauri stars (TTSs) are young,  $\lesssim 10 \,\mathrm{Myr}$  old,  $\lesssim 2 \,M_{\odot}$ , premain-sequence stars. Some TTSs, such as the classical TTSs, are still surrounded by dusty accretion disks, while others, the weak-lined or naked T Tauri stars (WTTSs), no longer retain their disks. Studying these young stars provides insight into the processes of stellar evolution and planet formation and the roles that disk accretion, nearby stellar companions, and strong stellar magnetic fields can play in these processes. Searching for planets in these young systems provides a snapshot of planet formation at its earliest stages. The radial velocity (RV) and transit methods commonly used to detect and analyze planets can be confused by spots on the surfaces of stars (e.g., Saar & Donahue 1997). As a result of their very strong magnetic fields and large spots (e.g., Johns-Krull & Herczeg 2007), this can be particularly problematic for young stars. A better understanding of the properties, including the lifetime, of star spots on young stars can aid in devising strategies to mitigate their effects and can provide insight into the dynamo processes that produce the spots in the first place.

Strong magnetic fields on young stars are of particular interest, as they contribute significantly to the star's environment and provide clues to the star's structure (Johns-Krull & Herczeg 2007; Mann et al. 2016). The appearance of large, long-lived spots on the surface of a star are hallmarks of such strong magnetic activity. In rapid rotators, spots tend to appear toward the poles, resulting in spot formations that can last for many years, as in V410 Tau, where a polar spot formation

persisted for at least 8 yr (Hatzes 1995; Stelzer et al. 2003), although this may not necessarily have been the same spot, but rather may have been similar-looking spot formations dispersing and reappearing at the pole (Hatzes 1995). Similarly, long-lived spots are described by Bradshaw & Hartigan (2014) on other young, rapidly rotating stars. Spots on the surface of slower rotators can remain in lower latitudes and contribute to measured Doppler variations of the stars' spectra more strongly than those at higher latitudes, but such spots are thought to rarely be coherent for much more than a year (Choi & Herbst 1996).

Hubble 4 is a WTTS in the Taurus-Auriga cloud. It is a highly magnetically active K7 star, with a mean surface field strength of 2.5 kG (Johns-Krull et al. 2004), and it was found to have large amplitude RV variations attributed to a spot (Mahmud et al. 2011). In much of the relevant literature, Hubble 4 is described as a single object; however, recent studies have shown it to be a close binary system (Kraus et al. 2011; Galli et al. 2018; Rizzuto et al. 2020). Hints of this binarity were reported earlier in a study of the radio emission from Hubble 4: Skinner (1993) found the emission was extended in such a way that might imply the presence of a companion. Kraus et al. (2011) reported that Hubble 4 is in fact a binary system based on Keck Observatory speckle imaging. They found that the system is composed of two stars, Hubble 4 A and Hubble 4 B, with a measured separation of approximately  $28.4'' \pm 0.1''$  ( $\sim 4.1$  au). Galli et al. (2018) used Very Large Baseline Array (VLBA) observations combined with near-infrared speckle interferometry of the system to determine dynamical masses for the two components,  $1.234 \pm 0.023 \, M_{\odot}$ for the primary and  $0.730 \pm 0.020 \, M_{\odot}$  for the secondary. The realization that Hubble 4 is a binary system is critical for interpreting RV variations of the unresolved system.

<sup>\*</sup> This paper includes data taken at The McDonald Observatory of The University of Texas at Austin.

We used RV data and Hubble Space Telescope (HST)/Wide Field Camera 3 (WFC3) photometry of Hubble 4, in conjunction with the system parameters reported by Galli et al. (2018) to study the RV variations produced by orbital motion and spot-induced signals. Removing the binary motion from the RV curve, we find a coherent star-spot signal in the RV data that has remained stable for at least 5.1 yr of observations, but less than  $\sim$ 12 yr. This paper is organized as follows: Section 2 presents the data used in the study, Section 3 presents the RV measurements made from the data, Section 4 presents the orbital fitting and spot analysis, Section 5 discusses a fortuitous flare captured in our data, and Section 6 presents our conclusions. Appendix A provides ancillary data tables and a full analysis of the HST imaging. A physically motivated RV model of the binary motion B that was used for the orbital RV subtraction in Section 4 is described in Appendix B.

## 2. Data

## 2.1. Imaging

We used the HST images taken through a variety of filters in late 2011 as part of program 12506 (PI: A. L. Kraus). These consist of three exposures through F275W, F336W, F390W, F395N, F438N, F475W, F555W, F625W, F656N, F775W, and F850LP. The binary was visible with a good signal-to-noise ratio in each exposure. We used the "\_flc" images for this analysis. These images have been bias subtracted and flat fielded. In addition, a pixel-based correction has been applied to each image to account for charge transfer inefficiency. A sample image, the third exposure with the F775W filter, is provided in Appendix B.1.

As described in Appendix B.1, we analyzed each exposure with an empirical point-spread function (PSF) that had been previously extracted from a set of dithered observations of the globular cluster Omega Centauri from program Cal-11452 (PI: J. Kim-Quijano). The many point sources in these images made it possible to construct an accurate model of the PSF, including its variation with position. To analyze each of the Hubble 4 exposures, we extracted a PSF tailored to the particular filter and to the binary's location on the WFC3/UVIS detector.

The three exposures for each filter were taken with the UVIS shutter in different positions. To account for the vibration-induced motion blur from the shutter in position B during shorter exposures (Hartig 2008), we applied a Gaussian blur to the PSFs. We used calibration data from Sabbi (2009) to determine that the best-fitting Gaussian kernel that describes that he camera jitter has an rms of 0.7 pixels and equal elongation in both directions. We applied the blurred PSFs to the exposures taken in shutter position B and applied the unblurred PSFs to exposures taken in shutter position A.

# 2.2. Spectroscopy

High resolution optical spectra were obtained using McDonald Observatory's 2.7 m Harlan J. Smith Telescope and the Robert G. Tull cross-dispersed coudé echelle spectrograph (Tull et al. 1995). Observations were taken between the years 2004 and 2018. Mahmud et al. (2011) analyzed the 26 observations taken between 2008 November and 2010 February. In addition to these, we also analyzed 20 observations taken between 2005 January and 2007 November as well as 20 observations taken between 2017 November and 2019 January. The dates of the observations are reported in Appendix A. Two observations had significant cloud or lunar contamination so we exclude these from the table in

Appendix A and from the analysis. A 1.2" slit was used to deliver a spectral resolution ( $R \equiv \lambda/\Delta\lambda$ ) of  $\sim\!60,\!000$ . The spectra, cross dispersed into 54–55 orders, were recorded on a Tektronix 2080 × 2048 CCD. Observations were made roughly once each night during a given observing run (typically 5–10 nights). Before and after each stellar spectrum, a Thorium–Argon comparison lamp spectrum was taken to determine the wavelength scale for the observations and detect any instrumental RV shift.

All spectra were reduced with a custom package of IDL echelle reduction routines based largely on the data reduction procedures described by Valenti (1994) and Hinkle et al. (2000). The reduction procedure is standard and includes bias subtraction, flat fielding by a normalized flat spectrum, scattered light subtraction, and optimal extraction of the spectrum. The blaze function of the echelle spectrometer is removed to first order by dividing the observed stellar spectra by an extracted spectrum of the flat lamp. Final continuum normalization was accomplished by fitting a second order polynomial to the blaze corrected spectra in the regions around the lines of interest for this study. The wavelength solution for each spectrum was determined by fitting a two-dimensional polynomial to  $n\lambda$  as function of pixel and order number, n, for approximately 1800 extracted thorium lines observed from the internal lamp assembly.

# 3. Spectroscopic Analysis

The main focus of the work presented in this paper is the analysis of the high resolution spectroscopy and the actual and apparent RV variations of Hubble 4 that it reveals. As described below, our observations imply long lifetimes for spots on the surface of young stars. The HST imaging analysis provides secondary information that complements the main analysis of this paper. Therefore, to preserve the flow of the main research presented here, the HST analysis and related results are presented in Appendix B.

# 3.1. RV Measurements

We determined the RV shifts of the various Hubble 4 spectra relative to one specific spectrum (Huerta et al. 2008; Mahmud et al. 2011). This reference spectrum was chosen as the observation with the highest signal to noise and the fewest noticeable cosmic ray hits that survived the reduction process. We chose as our reference the spectrum taken on 2007 February 10 (JD 2454141.6), shown in Figure 1. The number of spectral orders used in the analysis is between 9 and 11, depending on the quality of the individual spectra. For each observation, every useable order was cross correlated with the respective order in the reference spectrum (Tonry & Davis 1979). The cross-correlation function (CCF) between the reference and the observation was calculated and 11 pixels around the peak of the CCF were fit with a Gaussian to determine the RV shift at the subpixel level. The pixel shift was converted into a velocity using the wavelength dispersion and the Doppler formula. To account for any instrumental shift, a similar procedure was applied to the Thorium-Argon spectra taken before and after each observation and their shifts were averaged. This instrumental shift average and the barycentric velocity at the midpoint time of observation were then subtracted from the measured RV. The resulting value is the RV associated with a given order for a given observation.

The RV values for each order were then averaged, and the uncertainty in the final measurement was taken to be the standard deviation of the mean of the different RV values from each order,

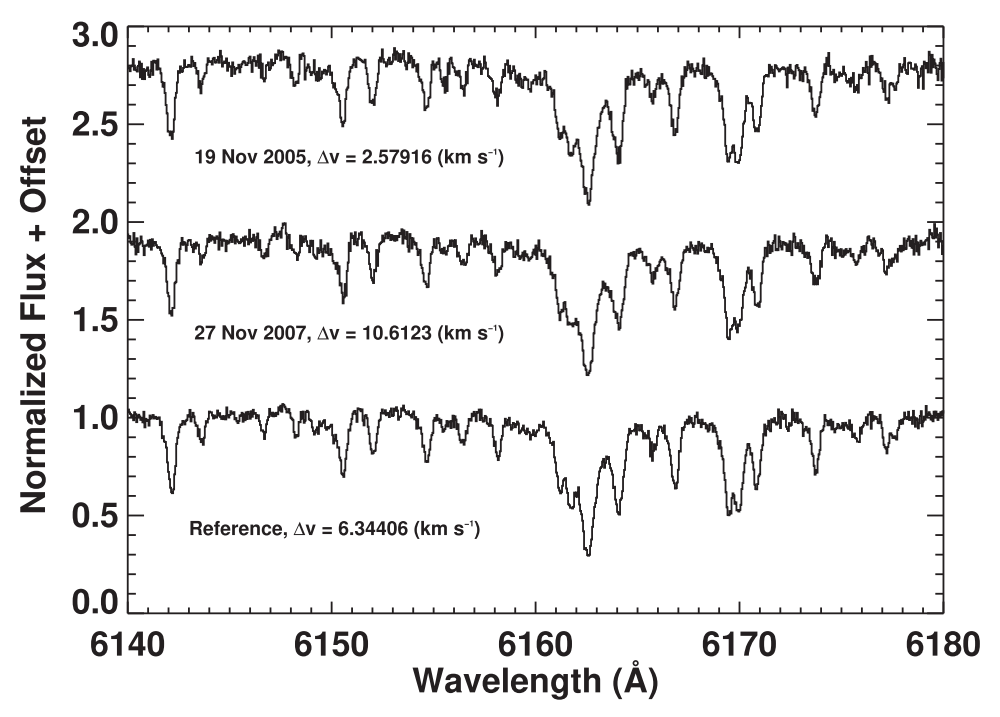


Figure 1. A portion of absolute order number 56 from three selected observations of the Hubble 4 system. The top observation was taken when the binary components were near minimum difference in their velocities. The middle observation was taken near the quadrature of the system, when the velocity difference between the components was greatest. The bottom is the reference spectrum, against which RV variations are measured.  $\Delta v$  denotes the predicted absolute velocity difference between the two components for each observation.

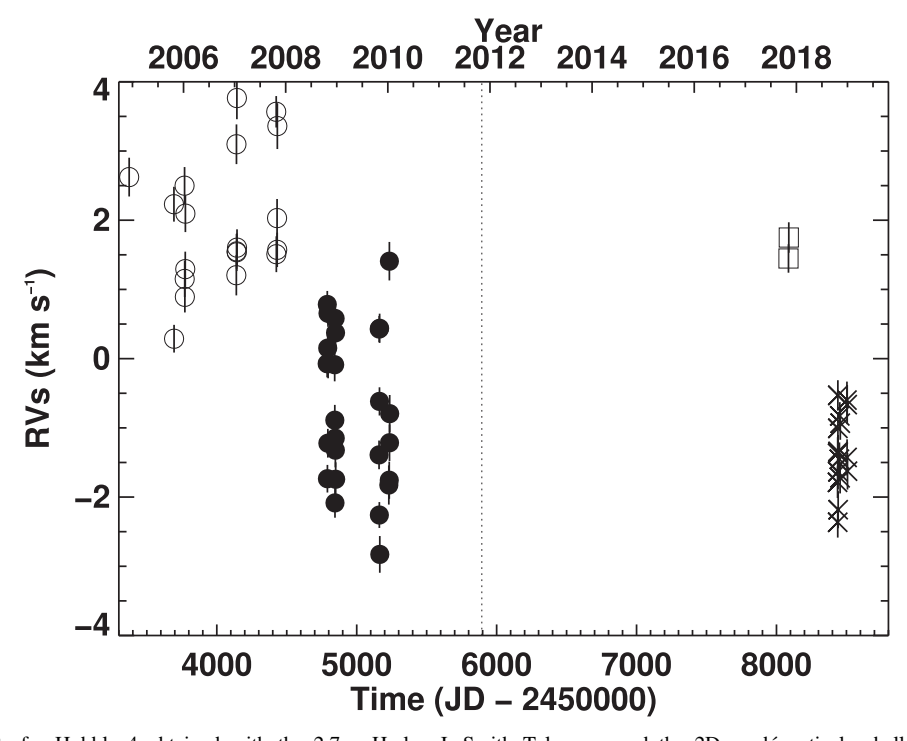


Figure 2. RV measurements for Hubble 4 obtained with the  $2.7 \,\mathrm{m}$  Harlan J. Smith Telescope and the 2D-coudé optical echelle spectrometer at McDonald Observatory. The 2005–2007 observations are shown with open circles, the 2008–2010 data with filled circles, and the 2018–2019 data with an  $\times$ . 2017 data that are not included in the analysis are shown with open squares. The dashed line indicates the date of the HST observations.

which was added in quadrature to the systematic uncertainty in the measurement ( $\sim$ 160 m s<sup>-1</sup>; see below). To estimate the systematic uncertainty, we applied the same procedure to known RV standards,  $\tau$  Ceti, 107 Psc, and HD 4628. These systems should not demonstrate any RV variation above 13 m s<sup>-1</sup> (Fischer et al. 2014), which is well below the precision we expect to obtain or

require. As a result, any variation measured in these RV standard stars can be attributed to systematic sources of uncertainty associated with our measurement technique. We take the mean of the standard deviations of the RV measurements of the three stars to be the systematic uncertainty. The RV measurements for Hubble 4 are shown in Figure 2 and given in Appendix A. The RV

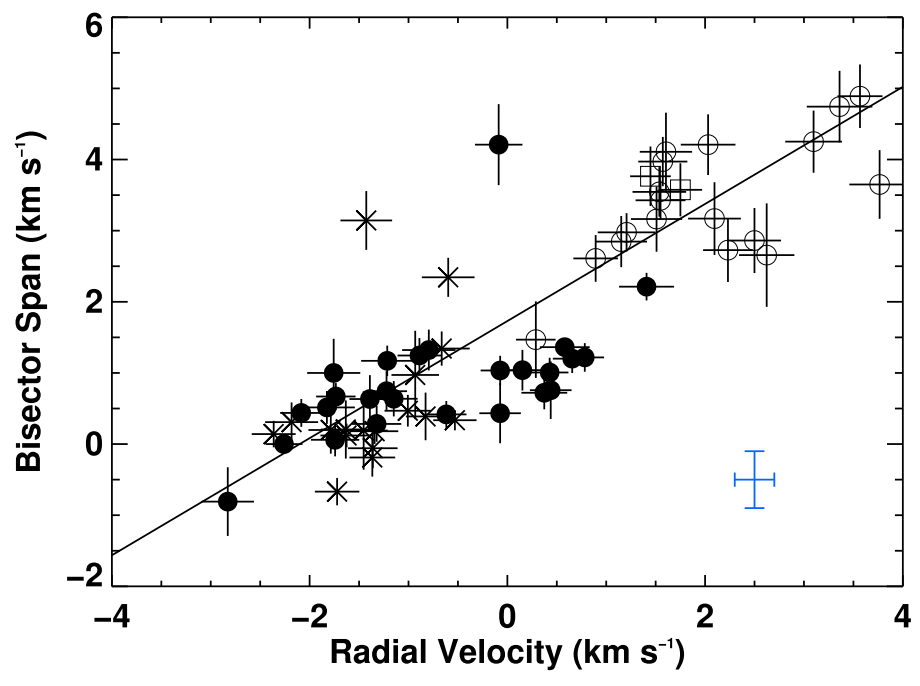


Figure 3. Plot of bisector spans vs. radial velocities. The 2005–2007 observations are shown with open circles, the 2008–2010 data with filled circles, and the 2018–2019 data with an  $\times$ . 2017 data that are not included in the analysis are shown with open squares. The line shows the best-fit linear correlation with a slope of 0.74 and a false alarm probability of  $2 \times 10^{-12}$ . The blue cross in the lower right corner shows a vertical uncertainty of 400 m s<sup>-1</sup> and a horizontal uncertainty of 200 m s<sup>-1</sup> to guide the eye.

values in this new analysis for the observations in common with Mahmud et al. (2011) closely match those reported in their paper. Subtracting one set of RV values from the other gives a mean difference of  $0~{\rm km~s^{-1}}$  with a standard deviation of the difference of  $200~{\rm m~s^{-1}}$ , which is within the final RV uncertainty achieved for our analysis.

### 3.2. Line Bisector Measurements

Star spots can cause spectral line deformations that can mimic RV variations in our measurements. Therefore, we are wary of any periods resulting from a periodogram analysis that are close to the stellar rotation period. Apparent RV variations at these periods might be caused by star spots carried across the surface by stellar rotation.

One way to quantify the deformations of spectral lines and to potentially identify signals resulting from star spots is to measure the line bisector spans (Huerta et al. 2008). The bisector is the set of points halfway between the two sides of a spectral line profile and the span is the inverse mean slope of the bisector. Rather than using individual spectral lines, we compute the bisectors of the normalized CCF used to measure the RV. The CCF can be considered an average inverse spectral line profile (Huerta et al. 2008). We take two points, one near the top of the CCF (mean of the bisector at CCF values 0.8 and 0.9) and one at the bottom (mean of the bisector at CCF values 0.15 and 0.25). The slope between these two points is then calculated. We compute the bisector span of the CCF for each order used to compute the RVs. The bisector spans are then averaged and we take the standard deviation of the mean to be the uncertainty in the span measurement. Strong correlation between the bisector span and the RV indicates that the apparent RV variations are likely caused by a spot rather than by a massive exoplanetary companion. Figure 3 shows the bisector span versus the RV and demonstrates

the strong correlation expected for spots. Bisector span measurements for Hubble 4 are given in Appendix A.

## 4. Spot-induced RV Variations and Spot Lifetimes

The goal of this paper is to study the lifetime of large star spots on Hubble 4 by observing the apparent RV signals produced by the spot(s) as the star rotates, following up on the results of Mahmud et al. (2011). However, the RV values that we measure in Hubble 4 have two sources: the spot-induced signals we wish to study and also signals resulting from the binary nature of the Hubble 4 system. The binary properties of Hubble 4 are well established (Galli et al. 2018; Rizzuto et al. 2020), therefore, for the purpose of this study, the binary signal needs to be subtracted out so that the spot-induced signals can be isolated and studied. This is done in a two-step process. To accurately fit the orbital contribution to the RV variations, the spot-induced signals need to be removed first through an approximate analysis of the different epochs of our Hubble 4 RV observations. Once the spot-induced RV signals are approximately removed, we perform an orbital fit to the residual RV variations. We then remove the orbital contribution from the original measured RVs and perform a more detailed analysis of the spot-induced RV signals.

The HST imaging allowed us to measure the optical flux ratio of the two members of the binary and that work is presented in detail in Appendix B (where it is also compared to the recent analysis of Rizzuto et al. 2020). The HST analysis shows that the optical flux ratio  $F_2/F_1$  is  $\sim$ 0.8, demonstrating that both stars contribute substantially to the observed optical light. This implies that the RVs resulting from the orbit of the binary represent the blending of spectral lines from the two sources. Because this binary has a long period,  $\sim$ 9 yr, and low orbital inclination (26°, Galli et al. 2018, Table 1), the RVs are low and the individual lines from each star never separate

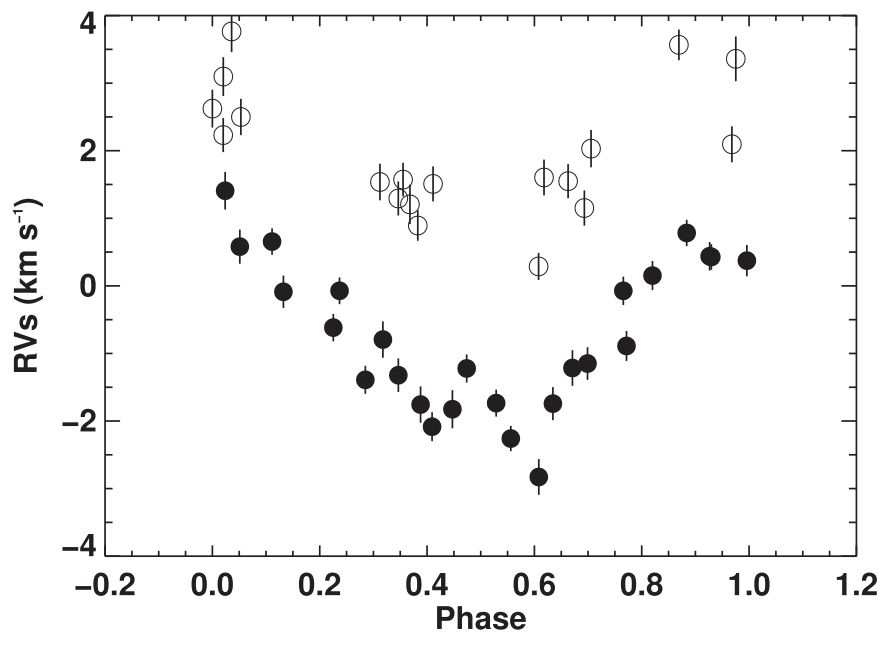


**Figure 4.** Observations from 2008–2010 and from 2005–2007 phase folded to a period of 1.5459 days. The two sets of measurements have a 2 km s<sup>-1</sup> shift between them. Observations from 2005–2007 are shown with open circles and observations from 2008–2010 are shown with filled circles.

Table 1
Hubble 4 Orbital Elements (Galli et al. 2018)

Parameter	Value	Uncertainty	
a (mas)	40.0	0.3	
$a_1$ (mas)	16.0	0.3	
$a_2$ (mas)	27.0	0.3	
$M_{\rm total}~(M_{\odot})$	1.964	0.033	
$m_1 (M_{\odot})$	1.234	0.023	
$m_2 (M_{\odot})$	0.730	0.020	
P (yr)	9.329	0.017	
$T_P$ (JD)	2454712	3	
e	0.682	0.003	
i (deg)	153.8	1.2	
$\Omega$ (deg)	66.1	2.3	
$\omega$ (deg)	70.0	2.2	

enough in velocity space to be clearly distinguished. The  $v \sin i$  of the components is also large,  $\sim 14 \, \mathrm{km \, s^{-1}}$ , compared to the maximum predicted velocity separation of  $\sim 10 \, \mathrm{km \, s^{-1}}$  captured in our observations (Appendix B.2). Appendix B presents detailed modeling of this line blending and the resulting RV signals.

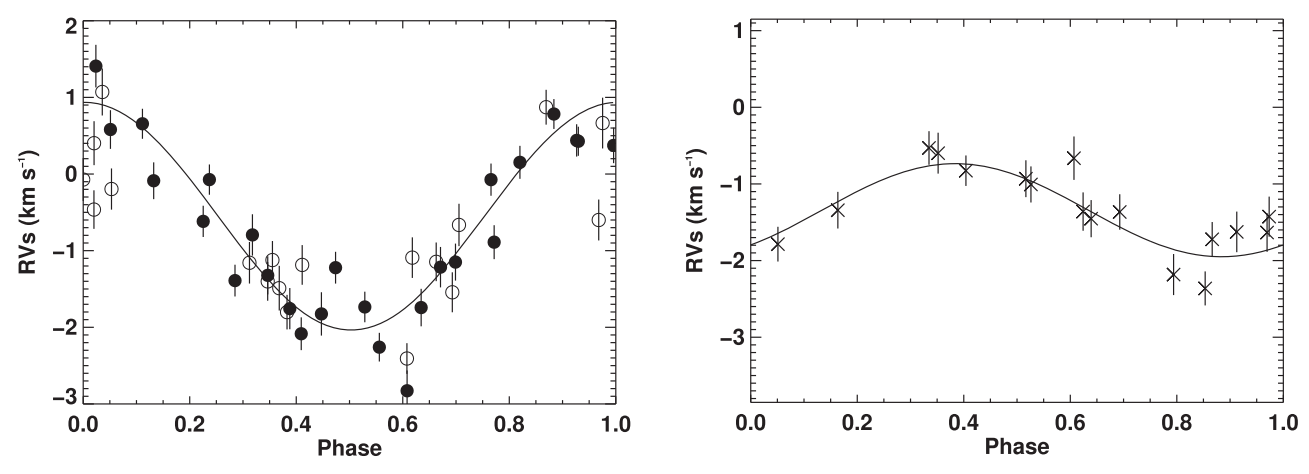
# 4.1. Spot Modulation and Orbit Fitting

Mahmud et al. (2011) analyzed 26 observations of Hubble 4 from 2008 November 17 to 2010 February 2 and found that the RV variations in the system were likely the result of the motion of a star spot across the surface of the star as it rotates. This conclusion was based on the short (1.5459 days) period of the RV variations, the apparent dependence of the amplitude of the variations on wavelength (infrared K band observations showed a noticeably smaller amplitude), and the strong correlation between the RV variations and the bisector spans. Photometric variations of the system's brightness also phased to the same period (Norton et al. 2007), strengthening the case for the presence of a spot. Modeling the spot on the surface of a star, assuming a photospheric

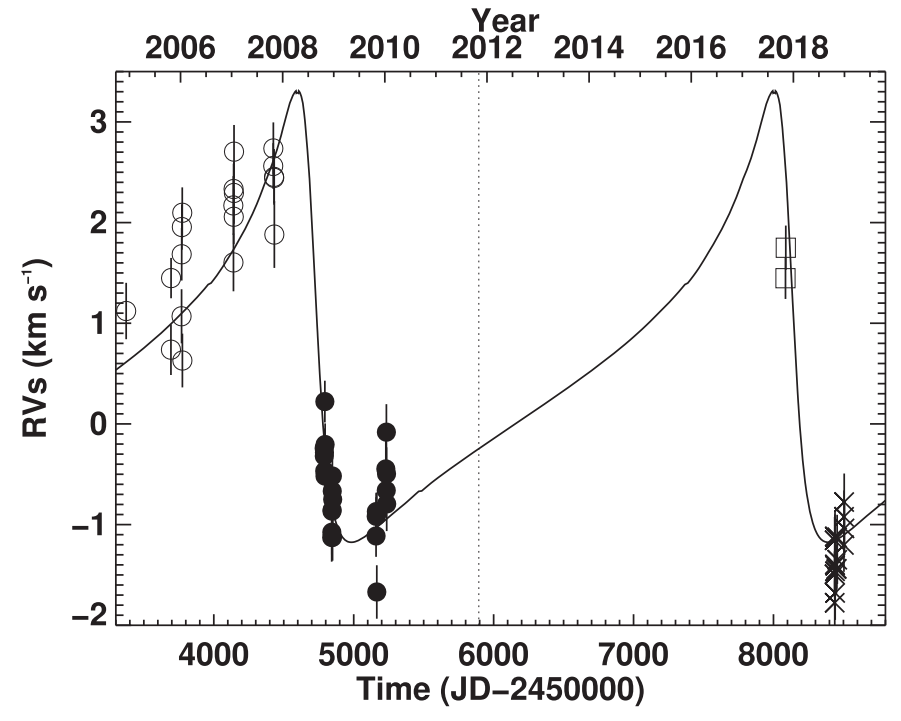
temperature of 4000 K and a spot temperature of 3000 K, confirmed that the presence of a large spot on a star with a rotation period of 1.5459 days could reproduce the observed RV semi-amplitude of  $1.395\pm0.094~\rm km~s^{-1}$  (Mahmud et al. 2011) in the optical. In Figure 4, the RV variations from 2008–2010 as well as from 2005–2007 are shown phased to the same 1.5459 day period.

Figure 4 shows that the 2005–2007 RV values are shifted roughly  $+2 \,\mathrm{km \, s^{-1}}$  relative to the later dates presented by Mahmud et al. (2011). There is a clear separation apparent for the bisector spans as well (Figure 3). Subtracting this apparent RV shift, the two sets of observations show coherent variations, as illustrated in the left panel of Figure 5. This implies that the spot responsible for the RV variations may have been stable for over 5 yr, a relatively long lifetime for a star spot although not unprecedented (Stelzer et al. 2003). The most recent data, from 2017–2019, also phase well to the 1.5459 day period but are not consistent in phase and amplitude with the older data (right panel of Figure 5). At first glance, this suggests significant spot evolution between the two epochs.

The simplest explanation for the RV offset seen in Figure 4 is an instrumental shift that is somehow unaccounted for by the Thorium-Argon spectra. However, a purely instrumental explanation is unlikely because it appears in the bisector spans as well (Figure 3). The bisector spans are computed differentially and do not depend on the absolute wavelength calibration. Thus, we conclude that the offsets in the RVs and bisector spans are real and potentially reflect the motion resulting from the longperiod binary. Galli et al. (2018) used their own VLBA observations combined with Keck/NIRC2 data (later published by Rizzuto et al. 2020) to determine the orbital motion of the binary and compute the orbital parameters of the system, summarized in Table 1. We use these parameters to fit the orbital contribution to the RV variations of Hubble 4. In order to isolate the orbital contribution from the spot-induced RV variation, we fit the two panels of data in Figure 5 with the simple sine waves shown in the plots and subtract these fits from the RV measurements in Figure 2. The two measurements from 2017



**Figure 5.** Two coherent spot signatures are present in the Hubble 4 RV data phased to a period of 1.5459 days. Solid lines show the sinusoidal fits to the spot-induced RV modulation, used to remove the spot signals from the full RV curve before modeling the binary. Left: mean-subtracted 2008–2010 data and mean-subtracted 2005–2007 data. The 2005–2007 observations are shown with open circles, and the 2008–2010 data are shown with filled circles. After subtraction of the means (difference of 2 km s<sup>-1</sup>), the two sets are indistinguishable. Right: data from 2018–2019 demonstrating a spot signal with the same period as the spot present in the 2005–2007 and 2008–2010 data, but shifted in phase and with smaller amplitude. Data from 2017 are not coherent with either spot signal and are omitted from these plots.



**Figure 6.** Filled circles show the Hubble 4 RV measurements after subtraction of the sinusoidal fits resulting from spot-induced apparent RV variations shown in Figure 5. The solid line shows the blended, double-line fit to the orbit using the parameters from Galli et al. (2018) described in Appendix B. The dotted line indicates the date of the HST observations. Though the 2017 data are shown in the figure for reference, they are omitted from the blended-line fitting procedure.

do not phase well with either spot signal, so they are omitted from the sine wave subtraction and spot fits shown in Figures 5 and 8. These initial spot-subtracted RV measurements are shown in Figure 6. We then fit a double-lined spectroscopic binary model to these RV measurements (Appendix B), holding the parameters fixed at the values given in Table 1. The only free parameters of the fit are the flux ratio of the components and their spectra line depth ratios. Due to the difficulty in phasing the 2017 data with the other RVs, we omit these points from the binary model fit. The observed RV variations actually result from the blended spectra of the two stars. Using the orbital parameters from Table 1 yields a peak-to-peak RV amplitude of  $\sim$ 8 km s<sup>-1</sup> for the primary and  $\sim$ 13.5 km s<sup>-1</sup> for the secondary.

The maximum predicted RV separation between the two components at the times we observed Hubble 4 is  $\sim 11 \, \mathrm{km \, s^{-1}}$ , which is less than the  $v \sin i$  of  $\sim 14 \, \mathrm{km \, s^{-1}}$  (see Appendix B.2) for the components. These predicted RV amplitudes are significantly larger than that seen in Figure 6, again, because the orbital signal seen in this figure results from the blending of the lines from the two components, and what we measure is the shift of the apparent velocity of these blended lines. We performed a double-lined analysis, described in Appendix B, and report those results there; this is shown as the solid line in Figure 6. We used a fit to our blended-line model to subtract the orbital motion from the RV variations shown in Figure 2 and used these orbital RV-subtracted data to

**Table 2**Sine Wave Fits to Spot Properties

Period	$A_1$ (km s <sup>-1</sup> )	$A_2$ (km s <sup>-1</sup> )	$ \Delta\phi $ (0.0–0.5)	$\chi_r^2$	$P_{\chi^2}$
$\overline{P_0}$	$1.146 \pm 0.062$	$0.496 \pm 0.103$	$0.377 \pm 0.040$	1.618	0.00253
$P_0 + \sigma_P$	$1.146 \pm 0.063$	$0.496 \pm 0.104$	$0.311 \pm 0.040$	1.642	0.00189
$P_0 - \sigma_P$	$1.145 \pm 0.063$	$0.496 \pm 0.103$	$0.443 \pm 0.040$	1.634	0.00210
$P_0 + 2\sigma_P$	$1.146 \pm 0.064$	$0.496 \pm 0.106$	$0.244 \pm 0.040$	1.709	0.00083
$P_0 - 2\sigma_P$	$1.145 \pm 0.064$	$0.496 \pm 0.105$	$0.490 \pm 0.041$	1.690	0.00104
$P_0 + 3\sigma_P$	$1.145 \pm 0.067$	$0.496 \pm 0.108$	$0.177 \pm 0.052$	1.819	0.00020
$P_0 - 3\sigma_P$	$1.143 \pm 0.066$	$0.496 \pm 0.108$	$0.423 \pm 0.042$	1.790	0.00030

further study the spot-induced RV signals of Hubble 4 (Section 4.2).

## 4.2. Spot Lifetime and Model Fits

Subtracting our blended-line binary model (solid line in Figure 6) from the observed RVs precisely removes the offset between the RV measurements shown in Figure 4 (Figure 8). This correction for the orbital velocity also appears to preserve the phase coherence of the spot-induced RV modulation observed in 2008–2010 compared to the 2005–2007 observations. This suggests that the spot or spot complex responsible for these RV modulations maintained its basic size and location for 5 yr (2005–2010) or more.

Data from 2018–2019 appear to phase well to the same rotation period as the earlier data, but there appears to be a significant phase shift (and amplitude change) compared with the 2005–2010 observations (Figure 5). To test whether this apparent phase shift is real, or whether a single period could be found that phased all the data together, we performed a dense search of nearby periods around the nominal rotation period (1.5459 days) in an effort to see if a single period could bring all the RV data into phase. The RV data appear very sinusoidal in nature (Figure 5), so we also evaluated different possibilities through a reduced  $\chi^2$  analysis of sine wave fits. As mentioned Section 4.1, the two data points from 2017 November do not appear to phase well with any of the other data, so we evaluate the fits without these two points.

The RV measurements from 2005-2010 provide more sensitivity to the rotation period than the 2018–2019 data because the earlier epochs have significantly more measurements (45 compared to 17) spread out over a significantly longer time interval (1862 days compared to 71 days). Therefore, we first determined how precisely we can measure the period using only the 2005–2010 data and then see how the later data phases to the range of allowed periods. To estimate the period in the 2005–2010 data, we performed 10,000 Monte Carlo simulations of the RV measurements, determining the period for each iteration. We performed two sets of Monte Carlo simulations: the first determined the period using the Lomb-Scargle periodogram (Horne & Baliunas 1986) and the second determined the period by minimizing  $\chi^2$  for a sine wave fit to the data points. For each iteration of the Monte Carlo runs, a new data set was created using the measured RV values and adding normally distributed random noise where the  $\sigma$  value from the normal distribution was set equal to the measurement uncertainty for the measured RV points. The best period estimate is taken as the mean of the 10,000 Monte Carlo runs and the period uncertainty is taken as the standard deviation of periods from the Monte Carlo runs. The Lomb-Scargle method

returned a period of  $1.545909 \pm 0.000042$  days and the minimizing  $\chi^2$  method returned a period of  $1.545900 \pm 0.000043$  days. We average these determinations to get a final period estimate of  $P_0 = 1.5459045 \pm 0.0000430$  days. The nominal period (1.5459 days) cited above (and used to compute the phases in Figures 5 and 8) is only  $0.1\sigma$  different than our new period,  $P_0$ . The 2018–2019 data is measured approximately 3000 days after the end of the 2005–2010 data. Using our new period and uncertainty, these 3000 days correspond to 1940 rotation periods and results in a potential phase error of 0.05, indicating that we can meaningfully test whether the two epochs maintain phase coherence.

It is clear in both Figures 5 and 8 that the 2018–2019 RV data points appear shifted in phase and have a substantially lower amplitude than the 2005–2010 data. In order to quantify the changes in phase and amplitude, we fit sine wave functions to the two sets of RV points, holding the period fixed to the same value for both fits. In order to evaluate the quality of the fits, we compute the value of reduced  $\chi^2$ ,  $\chi^2_r$ , as well as the probability,  $P_{\chi^2}$ , of obtaining the value of  $\chi^2_r$  this high or higher from a good fit to the data. When calculating these values of  $\chi_r^2$ we use the measured RV uncertainty values. However, as can be seen from the  $\chi^2$  values reported in Table 2, the values of  $\chi^2$ even for the best fit are a little high, indicating that either the measurement uncertainties are slightly underestimated (by a factor of  $\sim 1.27$ ) or that the spot-induced RV signal is not perfectly sinusoidal. Therefore, to quantify the uncertainty in the amplitude and phase of each sine wave, we multiply the measured uncertainties by a constant value equal to  $\chi_r$ —the square root of the reduce  $\chi^2$  value—so that the new value is  $\chi^2_r=1.0$ . In Table 2 we report the amplitude of the two sine waves,  $A_1$  (for 2005–2010) and  $A_2$  (for 2018–2019), as well as the absolute value of the shift in phase,  $|\Delta \phi|$  between the two sine waves. Table 2 provides the results of these fits for periods of  $P_0$  and  $P_0 \pm a\sigma_P$  for the values of a = 1, 2, 3. In all cases the amplitude of the two sine waves are significantly ( $\sim 5.4\sigma$ ) different and the phase difference is always greater than  $3\sigma$  (for  $P_0$  the phases are different at the 9.4 $\sigma$  level). The phases of the two sine waves are closest for a period of  $P_0 + 3\sigma_P$ , but they are still different at the 3.4 $\sigma$  level. Furthermore, the value of  $P_{\nu}^2$ indicates this fit is a factor of more than 10 less probable than the nominal  $P_0$  fit. As a result of all these tests, we conclude that the spot structure evolved significantly between the earlier and later epochs of RV data. While we cannot be sure the spot structure did not change appreciably during 2005-2010, the RV data we have collected are consistent with a very stable spot or spot complex during this time. Thus, we suggest that the lifetime of this spot or spot complex is at least as long as the time between the first and last observation in this period,

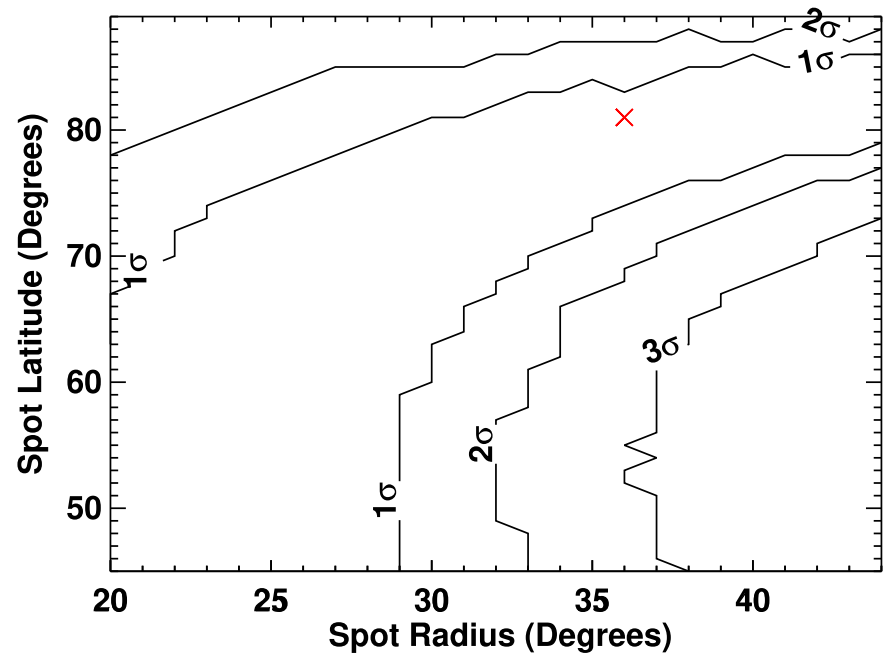


Figure 7. Contour plot showing  $1\sigma$ ,  $2\sigma$ , and  $3\sigma$  contours for the chi-squared surface for spot model fits to the 2005–2010 RV data. The radii and latitudes are sampled in increments of  $1^{\circ}$ . The red "x" marks the best-fit parameters.

corresponding to a minimum spot lifetime of  $\sim 5.1$  yr. Given the phase evolution of the spot in the later data, we can identify also an upper limit on the lifetime of this particular spot formation at  $\sim 12$  yr. This is consistent with the longest spot lifetimes observed on other young stars (Hatzes 1995; Stelzer et al. 2003; Bradshaw & Hartigan 2014; Robertson et al. 2020).

Since it appears that Hubble 4 has very long-lived spots on its surface, we investigated further the nature of these spots. We used the RV measurements to fit a spot model to the RV curve corrected for orbital motion. Applying a disk integration procedure similar to that described in Huerta et al. (2008), we determined the latitude, phase, and size of a single circular star spot that produces the best fit for the RV signal from 2005-2010, and we determined separate parameters for the spot from 2018-2019. To identify the best fit, we densely sampled a range of latitudes, phases, and sizes of a single circular spot and computed the chi-squared surface to identify the parameters at which chi-squared was minimum. For the inclination of the star, we adopted a value of 11.8°, computed assuming stellar radius of  $2.1 R_{\odot}$  from the Baraffe et al. (2015) isochrone for a 2 Myr old  $1.2 M_{\odot}$  star, a 1.5459 days rotation period, and a  $v \sin i$  of  $14 \, \mathrm{km \, s}^{-1}$  (see Appendix B.2). The stellar inclination we assume differs from the inclination of the orbital plane by  $\sim 14^{\circ}$ . While it might be expected that the orbital and stellar inclinations should be the same, a number of examples of binary young stars have been found where circumstellar disk inclinations are misaligned relative to the binary orbital inclination (e.g., Kurtovic et al. 2018), and circumbinary disks have been discovered that are misaligned relative to the binary orbit (e.g., Czekala et al. 2019). As a result, it appears that the minor misalignment we suggest for Hubble 4 is far from unique. While the phase is well determined, unfortunately the relationship between the latitude and size of the spot is highly degenerate as a result of the very low 11.8° stellar inclination, thus, there are multiple combinations of spot radii and latitudes that convincingly mimic the spot signal. The contour plot in Figure 7 demonstrates the

degeneracy between the choices of radius and latitude values to fit the 2005–2010 RV data. The formal best-fit parameters indicate a spot radius of  $36^{\circ}$  at a latitude of  $81^{\circ}$  for 2005–2010 (left panel of Figure 8). At that same latitude, the best-fit radius for the 2018–2019 spot is  $24^{\circ}$  with a shift of  $\sim 160^{\circ}$  in longitude (right panel of Figure 8). The spot coverage of the surface of the star from these spots agrees well with that found from the analysis of the HST imaging. We are confident that the more recent signal represents a smaller spot at any latitude and a longitude that differs by  $\sim 160^{\circ}$ . Completely different spot groups dominated on Hubble 4 during these two epochs.

One of the initial motivations for this study was to determine how long an individual spot or spot group on a TTS could last. This has bearing on any study that attempts to use RVs or photometric variability to detect planetary mass companions. In the case of Hubble 4, there is strong evidence that a large spot or spot group persisted in the same location on the star for at least 5 yr, which corresponds to  $\sim$ 1200 stellar rotations. This is much longer than spots last on the Sun; however, as discussed by Bradshaw & Hartigan (2014), such a long-lived spot on a TTS is not unexpected based on simple theoretical arguments. These authors examined the role of turbulent and magnetic diffusion in the decay of spots and show that for low gravity stars with strong magnetic fields and large spots (as is the case of TTSs), the decay time can be several years. In order to place Hubble 4 within this context, we must determine the spot's physical size. Assuming an angular radius of 36° from the spot modeling described above and a stellar radius of  $2.1 R_{\odot}$ , the spot has a physical radius of  $8.77 \times 10^5$  km. With a lower limit to the spot lifetime of 5.1 yr, we can recreate Figure 1 of Bradshaw & Hartigan (2014), placing Hubble 4 in the diagram as well. This is shown in Figure 9, where it can be seen that Hubble 4 lies close to HD 199178 and V410 Tau (Stelzer et al. 2003) and sits almost on the expected relation with a supergranule size of  $0.5 R_{\odot}$ . The first order explanation from this type of analysis is that large star spots live longer than smaller spots as is expected if a diffusion process governs their

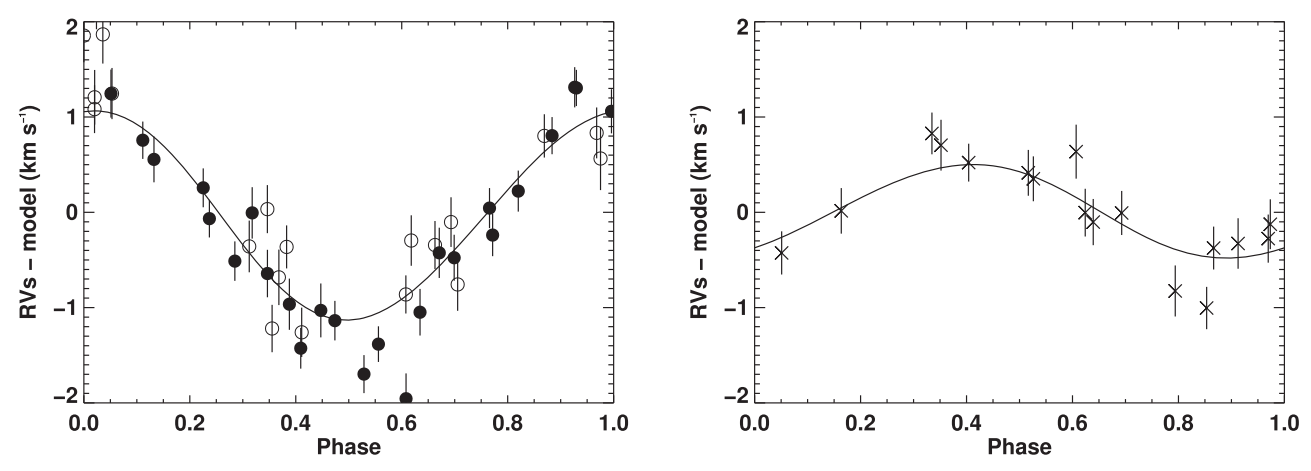


**Figure 8.** Orbital motion-subtracted RV curves for the observed spot signals. Left: the 2005–2007 data (shown with open circles) and the 2008–2010 data (shown with closed circles), which are almost indistinguishable after subtracting the binary RV contribution. The solid line shows a circular spot model assuming a radius of  $36^{\circ}$  on the star and a latitude of  $81^{\circ}$  overlaid with the RV data phased to P = 1.5459 days for the 2005–2010 spot. Right: spot model assuming a radius of  $24^{\circ}$  on the star and a latitude of  $81^{\circ}$ , in addition to a longitudinal shift of  $160^{\circ}$  (solid line) with respect to the 2005–2010 data overlaid on the 2018–2019 RV data phased to P = 1.5459 days.

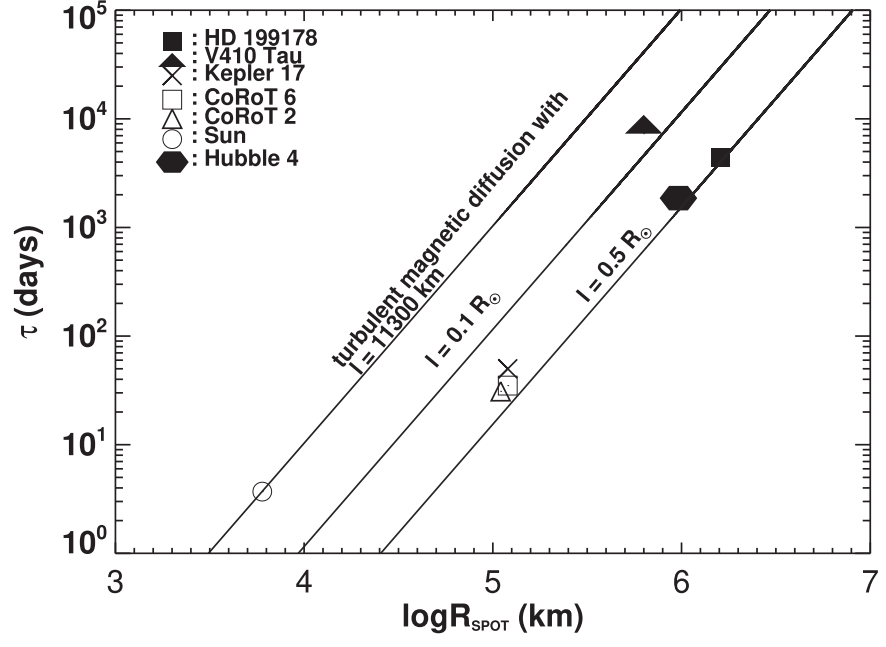


Figure 9. Observed spot durations and Gnevyshev-Waldmeier law (Gnevyshev 1938; Waldmeier 1955) models for varying super-granule sizes (Bradshaw & Hartigan 2014). The hexagon indicates the spot on Hubble 4 A, as it would appear in their original plot.

lifetimes. Bradshaw & Hartigan (2014) suggested that the solar and stellar data taken together support the idea that turbulent-driven magnetic diffusion governs the lifetimes of both sunspots and star spots and that supergranules represent the maximum scale size for this diffusion.

# 5. The Behavior of ${ m H}lpha$ and ${ m Two}$ Serendipitous Flares

One of the characteristic properties of magnetically active stars is chromospheric emission in the  ${\rm H}\alpha$  line, and WTTSs are no exception to this. On the Sun, chromospheric  ${\rm H}\alpha$  emission (really a filling in of the deep photospheric absorption line) is strongest in plages, which are most prominent in solar active regions. On active, late type stars of K and M spectral types, strong chromospheric activity produces  ${\rm H}\alpha$  lines in emission above the local continuum. The level of this chromospheric  ${\rm H}\alpha$  emission can vary on rotational and longer timescales as the

coverage of solar plage-like structures visible on the stellar surface changes, but it can also change dramatically on short timescales as the result of stellar flares.

Hydrogen lines can also be powerful probes of mass loss from gaseous exoplanets in close orbits around their host stars, so-called "hot Jupiters." Vidal-Madjar et al. (2003) were the first to use UV Ly $\alpha$  observations to detect mass outflow from a hot Jupiter; this has now been done for several of these objects (e.g., Ehrenreich et al. 2012). While most hydrogen-line observations of hot Jupiter mass loss have been done with Ly $\alpha$ , H $\alpha$  has also been used to study outflows from hot Jupiters (e.g., Cauley et al. 2017; Chen et al. 2020). H $\alpha$  emission from a young ( $\sim$ 2 Myr), evaporating hot Jupiter has also been reported (Johns-Krull et al. 2016). The authors found excess H $\alpha$  emission in WTTS PTFO 8-8695, which seems to move in velocity in phase with the period of a suspected planetary companion. The most likely explanation is that the emission

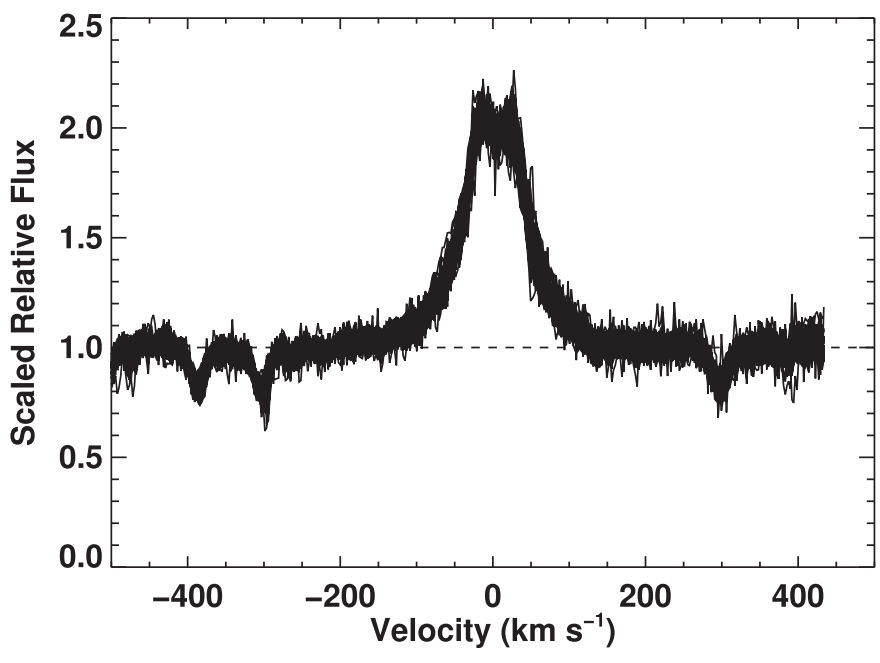


Figure 10. Overplotted H $\alpha$  emission lines from the 64 Hubble 4 system observations that do not contain a flare.

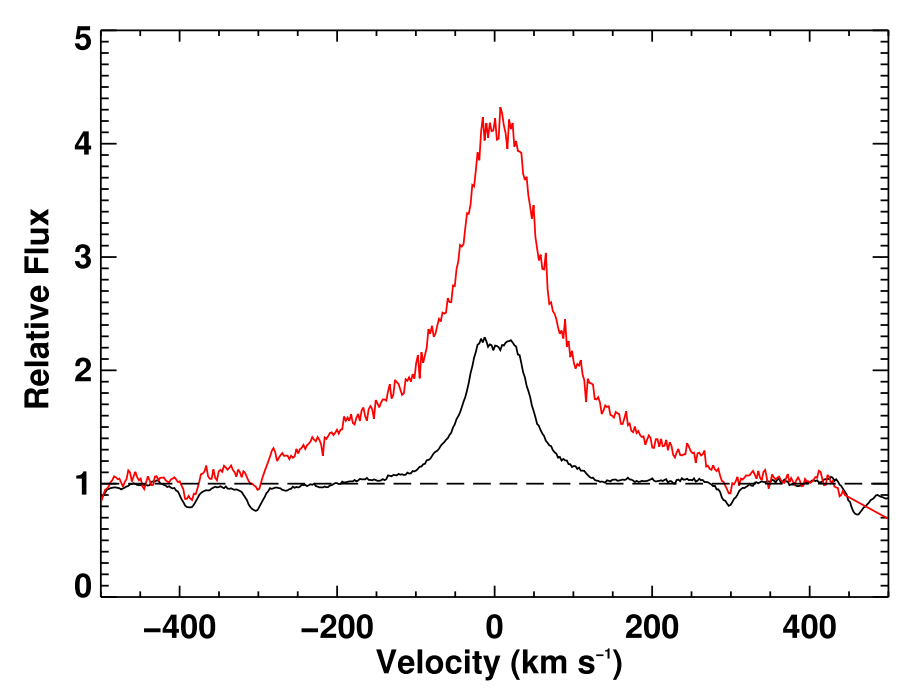


Figure 11. Relative flux of the  $H\alpha$  line for the very large flare (upper profile in red) compared to the average  $H_{\alpha}$  line profile in Hubble 4 for the UT 02:41:54.26 2007 February 13 flare. Dashed line at 1.0 for reference to continuum.

comes from the companion. However, as described in Johns-Krull et al. (2016), another possible source is stellar activity from the host star itself. Looking at the  $H\alpha$  profile variability of other WTTSs for similar effects will help determine the cause of the variations observed in PTFO8-8695. Specifically, we wish to see if the type of  $H\alpha$  variability seen in PTFO8-8695 (an excess emission component, nearly as strong as the central stellar component, observed to move from one side of the main line to the other) is commonly observed on other WTTSs.

We examined the H $\alpha$  line profile variations of Hubble 4. All but two of the line profiles display essentially the same shape, with variations appearing primarily as a scaling up or down of

the whole profile together. This can be seen in Figure 10 where we have scaled each profile so that the central 0.9 Å of the line has the same mean flux; none of the displayed profiles show a strong excess component out to  $\sim\!200\,\mathrm{km\,s^{-1}}$  on one side or the other as is seen in PTFO8-8695. Thus, the behavior seen in PTFO8-8695 does not appear to be present in Hubble 4.

We did, however, appear to catch two flares on Hubble 4, with one of them appearing to be quite powerful. The stronger flare was seen in the observation taken at UT 02:41:54.26 on 2007 February 13 (JD 2454144.62). Figure 11 shows the relative flux of the  $H\alpha$  line during this observation, as well as the average across all the other non-flaring observations. The

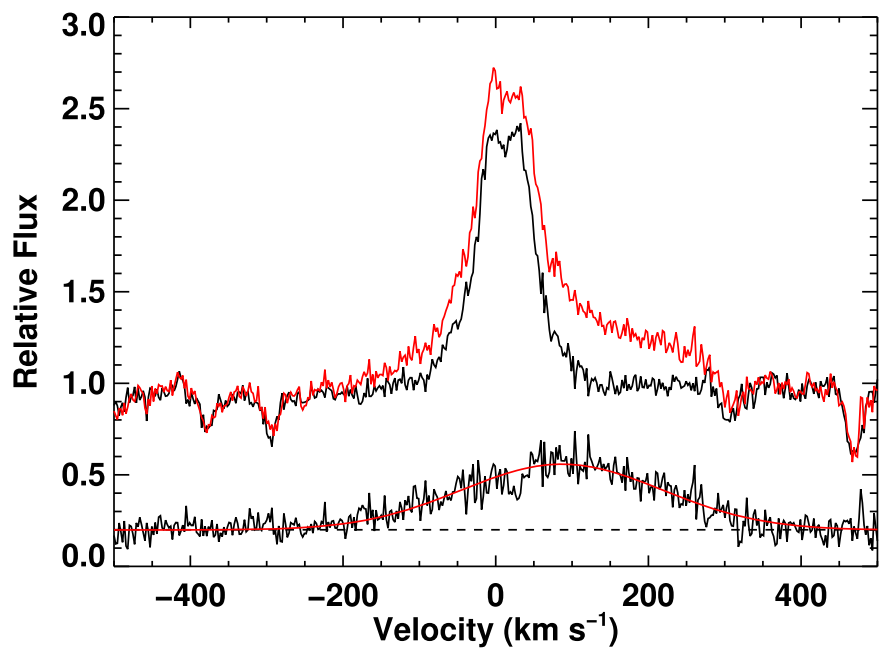


Figure 12. Relative flux of the  $H\alpha$  line for the UT 11:10:50.6 2018 November 17 flare (upper red profile) on Hubble 4 compared to the non-flaring  $H\alpha$  line profile (upper black profile) observed earlier the same night. The difference of the flaring minus the non-flaring profile (offset upward by 0.2 for clarity) is shown at the bottom (lower black profile) with a Gaussian fit (lower red, smooth line) overplotted. The dashed line provides the zero-point reference for the difference profile.

strong increase in emission with a roughly symmetric, substantial increase in the line broadening is a common feature of H $\alpha$  emission during flares on dMe stars (e.g., Honda et al. 2018; Vida et al. 2019). The measured equivalent width of the line was 13.43 Å during the flare, whereas the equivalent width of the average line is 2.99 Å, indicating an increase in the  $H\alpha$  emission by a factor of  $\sim$ 4.5 during the flare averaged over the 1800 s of this exposure. Assuming an approximate  $T_{\rm eff} = 4500 \, \rm K$  for the primary star and again using the BT-NextGen atmosphere models, the photospheric continuum spectral flux density at H $\alpha$  is  $\sim 2.3 \times 10^6$  erg cm<sup>-2</sup> s<sup>-1</sup> Å<sup>-1</sup>. Using a radius of  $2.1 R_{\odot}$  for the primary star and the measured increase in the equivalent width relative to the average for  $H\alpha$ , we calculated that this flare released a total of  $\sim 1.2 \times 10^{34}$  erg in the H $\alpha$  line alone during the portion of the flare we recorded. To estimate the total energy released in the flare during this time, we assumed the energy in  $H\alpha$  divided by the total *U*-band energy is ~0.06 (taken as a mean from flares studied in Kowalski 2012; Kowalski et al. 2013), and that the *U*-band energy divided by the total radiated energy is  $\sim 0.11$  (Osten & Wolk 2015). We then calculated a total flare energy of  $\sim$ 1.8 × 10<sup>36</sup> erg, significantly stronger than flare energies typically seen in dMe stars,  $\sim$ 10<sup>34</sup> erg captured across the entire visible range (Doyle et al. 2019). This is also  $\sim$ 10 times more energetic than flares reported on BP Tau (Gullbring et al. 1996). While our calculation of the flare energy is approximate, it is also a lower limit because we may not have captured the entire flare in our exposure, and we only consider the primary star when estimating the continuum flux density recorded. The secondary star has a projected separation of  $\sim$ 65 mas and is therefore well within our 1.2" slit and contributes its flux to the observed continuum.

A second flare was seen in the observation taken at UT 11:10:50.6 on 2018 November 17 (JD 2458440.95). On most nights during this run, we observed Hubble 4 twice: once at the beginning of the night and once at the end of the night. Figure 12

shows the relative flux of the H $\alpha$  line during the flare observation compared to the spectrum of Hubble 4 taken 7.3 hr earlier that same night when the star was not flaring. Again, we see an overall increase in the  $H\alpha$  line strength, including excess broadening in the wings. However, this time the observed excess is markedly asymmetric, with emission extending further to the red than to the blue. These types of asymmetric increases in emission are also commonly observed in flares from dMe stars (Honda et al. 2018; Vida et al. 2019). Simply subtracting the pre-flare profile from the flaring profile results in a profile that is very Gaussian in shape and displays a significant redshift (Figure 12). Redshifted emission components are often observed in both solar (e.g., Canfield et al. 1990) and stellar (e.g., Rice et al. 2011) flares. The redshifts are usually interpreted in terms of chromospheric evaporation and condensation that results from the intense heating of the upper chromosphere by downward propagating beams of electrons produced in the reconnection event that initiated the flare (Fisher et al. 1985a, 1985b). Fitting a Gaussian to the difference gives a velocity shift of  $+87 \,\mathrm{km \, s}^{-1}$  and an FWHM of  $310 \,\mathrm{km \, s}^{-1}$ . The equivalent width of the pre-flare H $\alpha$  profile is 3.02 Å, and the equivalent width of the flaring profile is 5.43 Å. The exposure time for the flare observation is again 1800 s. Using the same method as above to estimate the minimum total energy in this flare results in a value of  $4.1 \times 10^{35}$  erg, another very strong flare when compared to those typical of dMe stars.

# 6. Conclusion

We have analyzed RV data taken over a total of 14 yr for the WTTS Hubble 4 and combined this with an analysis of HST imaging of the system. The RV variations show clear contributions from both the 9.3 yr orbital motion of the binary system as well as a clear  $\sim 1.5$  day signal that is presumably the rotation period of the brighter component of the binary. The HST imaging data allowed us to estimate the separation, PA, and flux ratio of the component stars. The separation and PA

are consistent with the orbit determination presented by Galli et al. (2018). The flux ratio between the two stars (which affects the RV signal produced by the blended lines from the orbiting pair, and is therefore constrained by the measured RV signal) is consistent with the masses determined from Galli et al. (2018) and the 2 Myr isochrones from Baraffe et al. (2015) if we take into account that the primary is substantially spotted.

Subtracting the orbital contribution to the RV variations, we studied the spot-induced RV variations more closely. Our analysis shows that a large spot or spot group on Hubble 4 maintained its basic size and location on the surface for a minimum of 5 yr. Further, the size of this spot is consistent with the spot coverage needed to reconcile the imaging and orbital RV analysis of the flux ratio between the two components. Hubble 4's long-lived spot fits well with the turbulent diffusion analysis of spot sizes and lifetimes presented by Bradshaw & Hartigan (2014). These authors showed how spot sizes and lifetimes can be used to infer the size of supergranulation cells on stars, allowing studies such as the one we have presented here to inform stellar dynamo and flux emergence models. Equally important are the implications of our work for planet searches around very young stars. The primary planet search methods (RV and transit) must contend with the effects of star spots, which can produce astrophysical signals that mimic those of planets. The extremely long lifetime and large amplitude variations of coherent spots or spot structures on young stars can make it more difficult to search for planets around these stars. On the other hand, such stable structures offer possibilities to explore how to remove these signals using other measures of spot contributions, such as bisector span variations, and search for lower amplitude signals

from low mass companions (e.g., Donati et al. 2017). It is therefore important to use multiple criteria to rule out the potential effects.

We thank the anonymous referee for comments that improved the manuscript. This work was made possible in part by support from a Dessler Scholarship Grant through the Department of Physics and Astronomy at Rice University during the summer of 2017. Additional support for this research has been provided by the NSF through grant numbers AST-1461918 and AST-2009197 made to Rice University. We also acknowledge partial support provided by NASA through grant number 80-NSSC18K-0828 made to Rice University. Partial support for L. P. was provided by NASA Exoplanet Research Program grant 80-NSSC19 K-0289 and by the SIM Young Planets Key Project. This research was based in part on observations made with the NASA/ESA HST, obtained from the data archive at the Space Telescope Science Institute (STScI). STScI is operated by the Association of Universities for Research in Astronomy, Inc. under NASA contract NAS 5-26555. This research has made use of NASA's Astrophysics Data System Bibliographic Services. This research has made use of the SIMBAD database, operated at CDS, Strasbourg, France.

# Appendix A **RV** and Bisector Span Measurements

Table 3 presents the full set of RV and bisector span measurements obtained for Hubble 4.

Hubble 4 RV and Bisector Span Measurements

Civil Date	Julian Date (JD-2450000)	$\frac{\text{RVs}}{(\text{km s}^{-1})}$	$(\text{km s}^{-1})$	Bisector Spans (km s <sup>-1</sup> )	$\frac{\sigma_{\rm bisector}}{({\rm km~s}^{-1})}$
2005 Jan 3	3373.810	2.70	0.28	2.66	0.73
2005 Nov 19	3693.842	2.31	0.25	2.73	0.45
2005 Nov 20	3694.750	0.37	0.20	1.47	0.54
2006 Feb 3	3769.642	2.58	0.27	2.86	0.46
2006 Feb 4	3770.631	1.23	0.26	2.85	0.36
2006 Feb 5	3771.698	0.97	0.23	2.61	0.33
2006 Feb 8	3774.733	1.38	0.25	9.14	1.01
2006 Feb 9	3775.694	2.18	0.27	3.17	0.51
2007 Feb 8	4139.599	1.29	0.29	2.98	0.27
2007 Feb 9	4140.607	3.18	0.29	4.25	0.44
2007 Feb 10	4141.601	1.63	0.25	3.43	0.27
2007 Feb 11	4142.604	1.62	0.27	3.54	0.35
2007 Feb 12	4143.723	3.85	0.31	3.65	0.48
2007 Feb 13	4144.623	1.69	0.26	4.11	0.55
2007 Nov 20	4424.819	3.65	0.23	4.89	0.45
2007 Nov 21	4425.657	1.59	0.26	3.16	0.46
2007 Nov 26	4430.750	2.11	0.28	4.21	0.43
2007 Nov 27	4431.754	1.65	0.25	3.97	0.35
2007 Nov 28	4432.713	3.44	0.33	4.74	0.50
2008 Nov 18	4788.674	0.01	0.20	1.03	0.21
2008 Nov 19	4789.674	0.86	0.19	1.22	0.20
2008 Nov 20	4790.671	-1.65	0.20	0.67	0.19
2008 Nov 22	4792.667	0.23	0.22	1.04	0.29
2008 Nov 23	4793.678	-1.14	0.21	0.74	0.28
2008 Nov 24	4794.664	0.74	0.20	1.20	0.20
2008 Nov 25	4795.675	0.01	0.21	0.43	0.42
2009 Jan 11	4842.619	-0.01	0.24	4.21	0.57

Table 3

Table 3 (Continued)

(Continued)					
Civil Date	Julian Date (JD-2450000)	$RVs (km s^{-1})$	$(\text{km s}^{-1})$	Bisector Spans (km s <sup>-1</sup> )	$\sigma_{ m bisector} ({ m km \ s}^{-1})$
2009 Jan 12	4843.607	-0.81	0.22	1.25	0.25
2009 Jan 13	4844.593	-2.00	0.21	0.44	0.20
2009 Jan 14	4845.585	0.66	0.25	1.36	0.11
2009 Jan 15	4846.587	-1.07	0.24	0.64	0.25
2009 Jan 16	4847.588	-1.24	0.25	0.28	0.25
2009 Jan 17	4848.592	0.46	0.23	0.72	0.23
2009 Jan 18	4849.579	-1.66	0.24	0.06	0.23
2009 Nov 24	5159.765	-1.31	0.21	0.63	0.34
2009 Nov 25	5160.761	0.51	0.19	1.01	0.21
2009 Nov 26	5161.729	-2.18	0.19	0.00	0.00
2009 Nov 27	5162.764	-0.54	0.20	0.42	0.19
2009 Nov 28	5163.848	0.52	0.21	0.76	0.40
2009 Nov 29	5164.902	-2.75	0.27	-0.81	0.48
2010 Feb 2	5229.581	-1.74	0.28	0.52	0.23
2010 Feb 5	5232.581	-1.67	0.27	1.00	0.48
2010 Feb 6	5233.564	1.49	0.28	2.21	0.19
2010 Feb 7	5234.564	-1.13	0.26	1.17	0.21
2010 Feb 8	5235.564	-0.71	0.27	1.32	0.29
2017 Nov 28	8085.852	1.53	0.21	3.77	0.42
2017 Nov 30	8087.930	1.83	0.22	3.57	0.37
2018 Nov 14	8436.711	-1.70	0.23	0.20	0.33
2018 Nov 15	8437.703	-1.28	0.23	-0.19	0.27
2018 Nov 15	8437.951	-2.28	0.22	0.14	0.19
2018 Nov 16	8438.695	-0.45	0.22	0.34	0.14
2018 Nov 16	8438.991	-0.93	0.24	0.47	0.22
2018 Nov 17	8439.677	-1.55	0.25	0.21	0.41
2018 Nov 17	8439.977	-1.26	0.24	0.18	0.18
2018 Nov 18	8440.688	-1.28	0.25	-0.06	0.28
2018 Nov 18	8440.951	-2.10	0.27	0.31	0.28
2018 Nov 27	8449.987	-1.37	0.24	0.19	0.55
2018 Nov 30	8452.716	-0.75	0.20	0.39	0.33
2018 Dec 2	8454.977	-1.64	0.23	-0.67	0.19
2018 Dec 3	8455.981	-0.85	0.24	0.97	0.62
2019 Jan 20	8503.649	-0.52	0.27	2.34	0.27
2019 Jan 21	8504.610	-1.35	0.26	3.14	0.41
2019 Jan 22	8505.590	-0.58	0.28	1.34	0.24
2019 Jan 24	8507.608	-1.54	0.26	0.12	0.17

# Appendix B Double-line Spectroscopic Analysis for Fitting the Binary's RV Variations

Hubble 4 is a binary with a well-determined orbit (Galli et al. 2018) inclined to within  $\sim 26^{\circ}$  of face-on. The predicted peakto-peak RV amplitude of each star is  $\sim 8 \text{ km s}^{-1}$  for the primary and  $\sim 13.5 \text{ km s}^{-1}$  for the secondary. The maximum predicted RV separation between the two components at the times we observed Hubble 4 is  $\sim 11 \text{ km s}^{-1}$ , which is less than the  $v \sin i$ of  $\sim 14 \text{ km s}^{-1}$  (14.0 km s<sup>-1</sup>, see Appendix B.2). As a result, the measurement of the orbital-induced RV signal for this system represents the average of the two stars' motion captured by the blended-line profiles. These are mildly distorted as the result of the different continuum brightness and intrinsic line depth of the two components at different epochs. The CCF analysis of these profiles measured apparent RV variations that encode some of the orbital information, but the measured RV signal of these blended lines is not the true RV signal of either star. We modeled in a more physically motivated way the component RVs of the binary orbit to verify that we could reproduce our measured RV variations in a self-consistent

manner, while also verifying that the single-lined fit presented above effectively removed the orbital signal so that the spotinduced signal could be studied.

The model we explored was composed of two stars whose orbital parameters are taken from Galli et al. (2018). For each star, we created a model spectral line profile shifted in RV as dictated by the time of observation and orbital parameters. The line profiles for each component were added together to create a final "observed" line profile, which was analyzed in the same manner as the real observations to determine the RV for the observation. In order to add the profiles of the two stars we required the continuum flux ratio of the binary components, the intrinsic spectral line depth of each star, and the  $v \sin i$  of each star. We address each of these below and present our final orbital modeling in which we fit the spot-subtracted RV variations shown in Figure 6. While the  $v \sin i$  has been determined previously  $(14.6 \pm 1.6 \,\mathrm{km \, s^{-1}}; \,\mathrm{Johns\text{-}Krull} \,\mathrm{et} \,\mathrm{al}.$ 2004), we present a new determination of this quantity below. However, because we were not able to separate the spectral lines of the two components, we were not able to determine individual  $v \sin i$  values for the two stars. We assumed that the one value we determine (likely an overestimation given the line

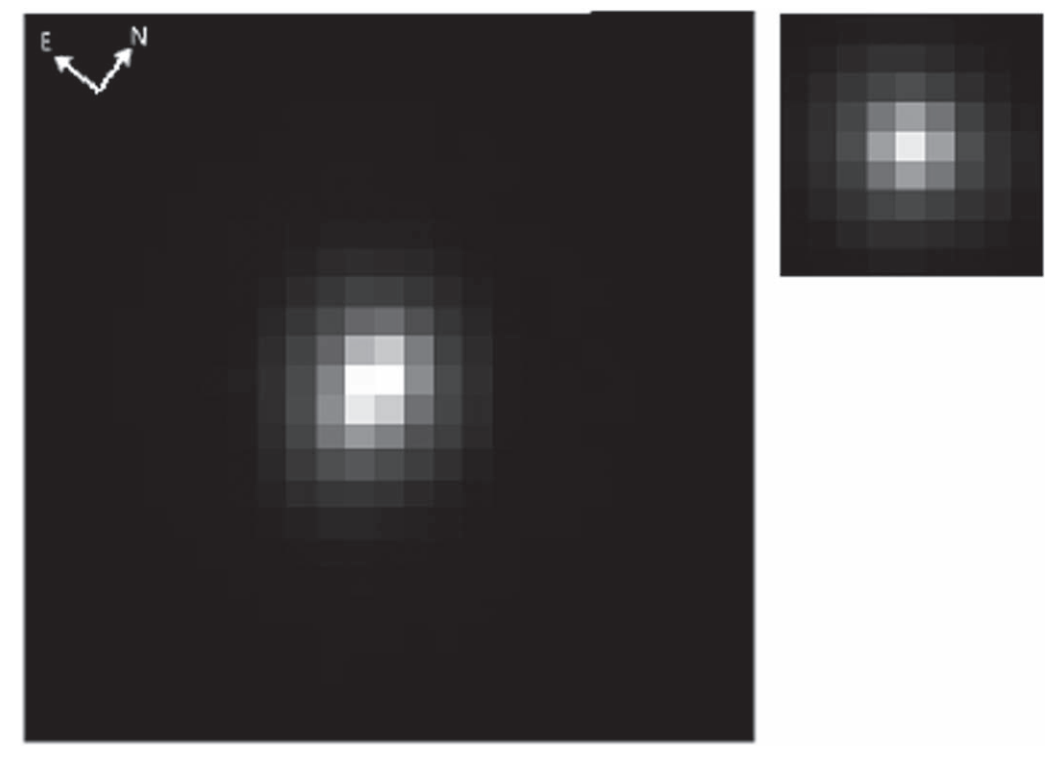


Figure 13. The third exposure taken on 2011 November 11, at UT 15:29:45 with the F775W filter on WFC3. The shutter is in the B position. The pixel scale is 0.04'' and the entire image is  $25 \times 25$  pixels, or  $1'' \times 1''$ . The PA of the binary is  $14^{\circ}$ . The Gaussian blurred PSF is shown in the upper right panel for reference, downsampled to match the resolution of the image.

blending) corresponds to the  $v \sin i$  of both stars. We were able to self-consistently model the RV variations of Figure 6 using the known orbital parameters from Galli et al. (2018), suggesting that our treatment of  $v \sin i$  did not cause serious discrepancies.

## B.1. HST Imaging of the Binary

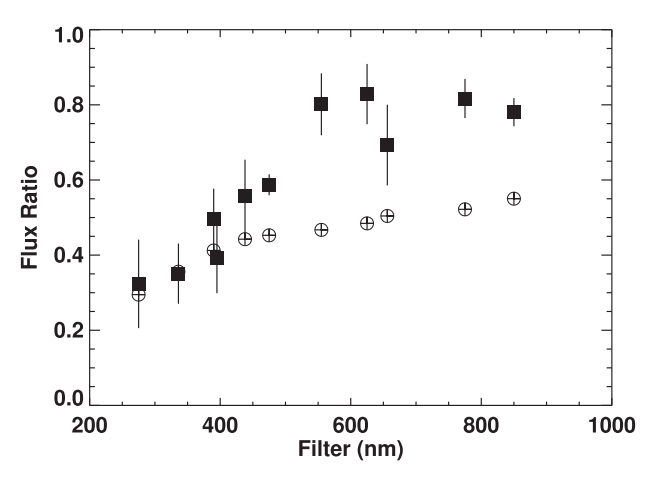
We relied on the HST imaging to determine the flux ratio of the two stars in the Hubble 4 system. An example image, the third exposure with the F775W filter, is shown in Figure 13. In order to measure the relative flux ratios in the 11 HST WFC3 filters, we applied a least-squares fitting approach to the individual images. The parameters we varied were the horizontal and vertical positions of the components and their relative flux. Given the proximity of the components, there was a high degree of degeneracy between the relative stellar fluxes of the two and their positions. In order to resolve the degeneracy, we established a center of mass analog, which we call the center of flux. The center of flux in each of the filters was determined by a single source fit with an oversampled PSF including a Gassian blur in one of the two shutter positions because of the short exposure times (see Section 2.1). We varied the position and overall flux of a single source using our PSF, which was then binned to the observed pixel scale in order to create a model image. We then determined the position that minimized the squared difference between the model and observed image.

The two-source fitting via least squares with an oversampled PSF was then combined with the center of flux determined from the single source fit and the separation between the sources in the horizontal and vertical directions was varied. A region of  $9 \times 9$  WFC3 pixels was cut out of each image around the center of flux location. The CCDs in the UVIS channel of WFC3 have pixels that are 0.04'' on a side, so the extracted

**Table 4** Hubble 4 Photometric Model Results

	Exposure Time	Separation	PA		D' 1 D
Filter	(s)	(mas)	(deg)	Flux Ratio	Final Flux Ratio
F275W	100	$61^{+8}_{-12}$	$5^{+15}_{-17}$	$0.281^{+0.431}_{-0.258}$	$0.323^{+0.117}_{-0.099}$
F336W	25	$65^{+6}_{-12}$	$18^{+8}_{-7}$	$0.309^{+0.288}_{-0.199}$	$0.351^{+0.080}_{-0.071}$
F390W	8	$65^{+5}_{-8}$	$18^{+5}_{-6}$	$0.411^{+0.246}_{-0.183}$	$0.495^{+0.081}_{-0.074}$
F395N	100	$61^{+3}_{-8}$	$14^{+7}_{-6}$	$0.389^{+0.259}_{-0.185}$	$0.393^{+0.094}_{-0.083}$
F438W	4.5	$70^{+5}_{-11}$	$20^{+6}_{-7}$	$0.440^{+0.376}_{-0.248}$	$0.556^{+0.098}_{-0.087}$
F475W	1.0	$64^{+3}_{-5}$	$12^{+2}_{-3}$	$0.549^{+0.109}_{-0.076}$	$0.587^{+0.028}_{-0.027}$
F555W	0.48	$71^{+3}_{-5}$	$17^{+5}_{-5}$	$0.722^{+0.378}_{-0.269}$	$0.801^{+0.082}_{-0.076}$
F625W	0.48	$71^{+4}_{-5}$	$15^{+4}_{-3}$	$0.734^{+0.555}_{-0.331}$	$0.829^{+0.080}_{-0.074}$
F656N	9.0	$71^{+6}_{-9}$	$18^{+6}_{-7}$	$0.539^{+0.604}_{-0.340}$	$0.693^{+0.107}_{-0.095}$
F775W	0.48	$69^{+5}_{-6}$	$14^{+4}_{-3}$	$0.741^{+0.134}_{-0.179}$	$0.817^{+0.052}_{-0.049}$
F850L	0.80	$65^{+3}_{-3}$	$14^{+3}_{-2}$	$0.773^{+0.135}_{-0.083}$	$0.781^{+0.037}_{-0.036}$

regions were 0.36'' on a side. The nominal FWHM of the UVIS PSF is  $\sim 0.075''$  or narrower in the bands observed. We first normalized the observed image subregion by the total flux because the PSFs used were normalized to unit total flux. Each of the two sources was assigned a relative flux, the brighter given by F,  $0.5 \le F \le 1.0$ , and the dimmer given by 1 - F. Then shifting the brighter source by ((1 - F)dx, (1 - F)dy) relative to the center of flux and the dimmer source by (-Fdx, -Fdy) relative to the center of flux, with F greater than 0.50 to prevent degenerate solutions, the binary was reproduced by finding the best-fit parameters F, dx, and dy, which minimized  $\chi^2$  between the model and observed images. Table 4 provides the results of the least-squares fitting for the 11 filters, where



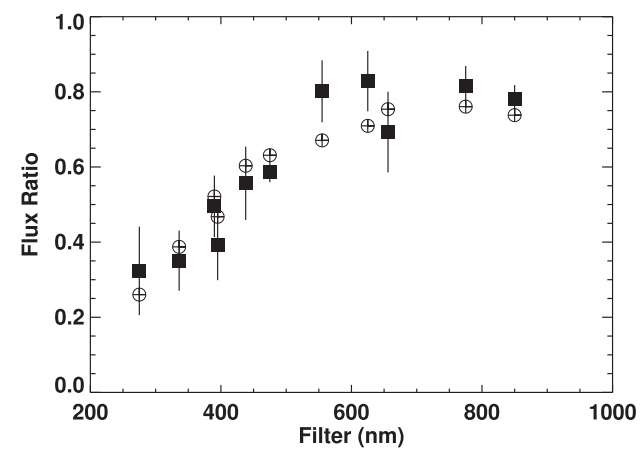


**Figure 14.** Left: filled squares represent flux ratios from best fit of images, circles with crosses show flux ratios for NextGen spectra assuming no spot coverage. Right: filled squares represent flux ratios from best fit of images, circles with crosses show flux ratios for NextGen spectra assuming 60% spot coverage of the primary, 0% spot coverage of the secondary.

the flux ratio is defined as (1-F)/F and is the flux of the secondary divided by the flux of the primary. The PAs of the secondary relative to the primary describe the projected position of the binary in the plane of the sky measured in degrees east of north. The PAs and separations are relatively consistent across filters. The mean separation and PA (and their mean uncertainties) of the components are found to be  $66.7 \pm 7$  mas and  $15^{\circ} \pm 6^{\circ}$ , respectively. For the date of the HST observations, the orbital parameters from Galli et al. (2018) predicted a separation of  $62.86 \pm 1.27$  mas and a PA of  $13.98^{\circ} \pm 5.14^{\circ}$ , showing that our results are fully consistent the Galli et al. (2018).

In reality, the relative position of the two sources should not depend on the wavelength of observation. Since our separations and PAs are consistent with those of Galli et al. (2018), we analyzed the images again, holding these parameters fixed at the Galli et al. (2018) values, and solve only for the flux ratio. The resulting ratios are given in the last column of Table 4 and are plotted in Figure 14. Generally, the two stars are more similar in brightness at redder wavelengths than they are in the blue, indicating that the secondary component is cooler than the primary, as expected for the more massive primary. The flux ratios in the visible filters (F555W, F625W) have an interpolated value of  $0.80 \pm 0.08$  at the mean wavelength used for the RV analysis (5594 Å) described below.

To test how these flux ratios compare with those predicted by current young star models, we took stellar parameters from Baraffe et al. (2015) isochrones using the masses from Galli et al. (2018) and reported in Table 1 at an assumed age of 2 Myr. These models give effective temperatures and radii of 4530 K and 2.1  $R_{\odot}$  for the primary and 4070 K and 1.7  $R_{\odot}$  for the secondary. We used synthetic spectra from the NextGen model atmospheres (Hauschildt et al. 1999) to compute predicted flux ratios. Specifically, the BT-NextGen low resolution synthetic spectra (Allard et al. 2012) with the Asplund et al. (2009) abundances at a variety of temperatures. We varied the effective temperature between 3800 and 4300 K for the secondary and between 4500 and 4800 K for the primary to estimate the predicted flux ratios. The synthetic spectra were multiplied by the HST WFC3/UV-vis passbands (Kalirai et al. 2009),

integrated, and scaled according to the assumed radii for each component. The flux ratio of the system in each of the bands was then determined for the assumed temperatures. While the extinction to Hubble 4 is generally considered to be low, we assumed it was the same to each component and thus did not take it into account to estimate the flux ratios. The combination of temperatures that yielded the most similar flux ratio curve to that of the observations is 4500 K for the primary and 4300 K for the secondary (left panel of Figure 14). Clearly, the model flux ratio curve is discrepant with respect to the observations, and the parameters have each gone to limits we imposed to force the temperatures of the stars as close together as the fitting allowed. This is because the ratio of surface areas for the stars is 0.66, which is then the largest the flux ratio could be if the stars had the same temperature. As long as the less massive star is cooler, the ratio will be smaller, and as a result will not provide a good fit to the observed flux ratios. Either the relative radii of the two stars are poorly predicted by the Baraffe et al. (2015) models, or some other effect must be considered.

To attempt to better approximate the flux ratio curve, we allowed the two components to have large star spots. We used NextGen spectra for the predicted effective temperatures, 4530 and 4070 K (Baraffe et al. 2015). We assumed the spot temperatures are 1000 K less than those of the photospheres (e.g., Bouvier et al. 1993) and added these to the spectra of the components at varying filling factors. We held the unspotted photospheric temperatures at the values found above. This results in a much better fit, as shown in the right panel of Figure 14. The resulting best-fit spot coverage was 60% on the primary with the secondary unspotted. While this was crudely estimated, it appears that pre-main-sequence models can reproduce the HST photometry if we allow for large spot coverage on at least the primary. Although it is unlikely that the secondary is entirely unspotted, the dominant flux of the primary drives the fit to suppress any spot contribution from qthe secondary. The assumption of large spot coverage on the primary explains the greater flux ratios found in the redder wavelengths here, as well as in the NIR as discussed in Rizzuto et al. (2020).

## B.2. Optical v sin i Measurement

We attempted to disentangle the RV signals resulting from the binary motion from those produced by star spots by

Obtained from http://svo2.cab.inta-csic.es/theory/newov/.

Obtained from http://www.stsci.edu/hst/instrumentation/wfc3/performance/throughputs.

modeling the observed line profiles as the sum of spectral lines from the two stars. Such modeling requires an estimate of the  $v \sin i$  of the two sources. As the spectral lines from the two stars are far from resolved, we estimated a single  $v \sin i$  value by analyzing the observed profiles as if they come from only one source and then assumed that the two stars have the same  $v \sin i$ . Our resulting estimate of the  $v \sin i$  is therefore likely an overestimation compared to the true rotation rate.

The  $v \sin i$  values were measured using the same general technique outlined in Hartmann et al. (1986) and Soderblom et al. (1989). The premise of this method is that the FWHM of an appropriate mean line profile is directly proportional to the  $v \sin i$  of the star. In many cases, the mean line profile used is the CCF, created when the target star spectrum is cross correlated against an unbroadened, narrow-lined spectrum. Another suitable mean line profile that can be used results from applying the technique of least-squares deconvolution (LSD; Donati & Cameron 1997) to dramatically boost the signal to noise of individual observations. For this paper, LSD line profiles were constructed using the line list and code described in Chen & Johns-Krull (2013). Using this method to measure  $v \sin i$  requires that we first calibrate the relation between the FWHM of the LSD profile and the  $v \sin i$ . In order to do this, we used the observed spectrum of a slowly rotating star of similar spectral type to Hubble 4.

HD 65277 is classified as a K4 dwarf star (Houk & Swift 1999). Using the spectral type to effective temperature calibration for dwarf stars from Pecaut & Mamajek (2013), this spectral type implies an effective temperature of 4620 K. Valenti & Fischer (2005) included HD 65277 in their spectroscopic analysis of 1040 F, G, and K dwarfs, and found an effective temperature of 4741 K and a  $v \sin i = 1.0 \, \mathrm{km \, s^{-1}}$ . The recent spectroscopic analysis of Soto & Jenkins (2018) identified a stellar  $T_{\rm eff} = 4660 \pm 14 \, \mathrm{K}$  for HD 65277 along with a rotational velocity of  $v \sin i = 1.81 \pm 0.08 \, \mathrm{km \, s^{-1}}$ . As these estimates of the rotational velocity are below the resolution (2.5 km s<sup>-1</sup>) of our optical data, HD 65277 serves as essentially a nonrotating template with a spectral type very similar to that of Hubble 4.

To construct the relationship between the FWHM of the LSD profile and the stellar  $v \sin i$ , we artificially broadened the observed spectrum of HD 65277 with a standard rotational broadening kernel (Gray 2005). We then computed the LSD profile of this rotationally broadened spectrum and measured the FWHM of the LSD profile. This procedure was repeated for several values of  $v \sin i$  to produce a calibration curve for the data. We then used the Hubble 4 LSD profile of each observation and linearly interpolated on the calibration relationship to get a  $v \sin i$  measurement for each observation. We then took the mean of the different  $v \sin i$  values as our final estimate of the rotational broadening. We also computed the standard deviation of the mean for the multiple  $v \sin i$  values and assumed this to be the random uncertainty associated with our measurement. We estimated the systematic uncertainty in our analysis by using two additional slowly rotating stars (HD 80367 and HD 88371 with  $v \sin i$  values of 1.9 and 1.4 km s<sup>-1</sup>, respectively; Valenti & Fischer 2005) as templates. We achieved agreement between the  $v \sin i$  measurements made with the three templates to typically better than  $0.7 \,\mathrm{km \, s^{-1}}$ , which we took as our systematic uncertainty and added in quadrature to the random uncertainties. Our final  $v \sin i$ estimate for Hubble 4 was  $14.0 \pm 0.8 \,\mathrm{km \, s^{-1}}$ , which we

assumed to be equal for both the primary and the secondary. This value is within errors of other previous measurements (e.g., Johns-Krull et al. 2004).

## B.3. Modeling of the Hubble 4 Orbital RV Variations

We modeled the orbital contribution to the RV variations of Hubble 4 by constructing synthetic line profiles of the system and analyzing them in the same way as the observations. We created a template line profile for each component of the binary and added them together, taking into account continuum brightness differences and RV offsets of the two components to create each epoch's "observed" line profile. The data we try to reproduce are the initial spot-subtracted RV measurements shown in Figure 6. As in the spot fits, we omit the 2017 data from those used to constrain the double-lined binary model. The LSD line profile of HD 65277 was used as the template to model the spectral line profiles of each component.

In order to model the binary, the predicted RV values of each component, based on the orbital parameters given in Table 1, were computed at each observing epoch. We assumed the two stars had the same  $v \sin i$ ,  $14.0 \,\mathrm{km \, s^{-1}}$ , and then rotationally broadened the template by this amount. We made two copies of the broadened template, and shifted the broadened template by the RV values of the two stars (Figure 15). Leaving the Hubble 4 A profile normalized to 1.0 in the continuum, the Hubble 4 B profile was then multiplied by a flux ratio, f. The two profiles were then added together and renormalized by 1 + f, and all of the resulting profiles were cross correlated with the single rotationally broadened template to measure the resulting RV value. These model RVs were then fit to the observed RVs, and reduced  $\chi^2$  minimization was used to find the flux ratio that best fit the observations, resulting in  $f = 1.07^{+0.05}_{-0.04}$ . This differs significantly from the best-fitting flux ratio (0.80) in the HST photometric data discussed above and implies the secondary is brighter than the primary. We then tried fixing the continuum flux ratio to 0.80 and then varied the ratio of template line depths between the primary and secondary component and refit the observations. We found a line depth ratio of  $0.61 \pm 0.03$ (i.e., the lines of the primary are 61% as deep as those of the secondary) brings the RV model in agreement with the imaging data. Deeper lines in the secondary better match expectations. The cooler chromosphere of the secondary would absorb more of the blackbody core emission than the hotter primary's chromosphere. An example set of line profiles used in the final modeling is shown in Figure 15. The orbital RV model fit based on the LSD analysis is shown in Figure 6.

To investigate whether the final line ratio we found for this system is reasonable, we used the Vienna Atomic Line Database (VALD; Piskunov et al. 1995; Ryabchikova et al. 2015) to extract spectral line data and synthesize models of the two components, assuming effective temperatures of 4400 K for component A and 4000 K for component B (these temperatures correspond to the models in the NextGen grid that are closest in effective temperature to the predicted temperatures found for each star). A surface gravity ( $\log g$ ) of 3.5 is assumed, as described in Johns-Krull et al. (2004). We used the synthesized spectra to compute LSD line profiles for the two effective temperatures and employed the VALD line list covering the same wavelengths used to measure the RV and bisector span for the actual observations. The spectra synthesized from these models indicated a line depth ratio of 0.91. Although this ratio is in the correct sense (the lines of the

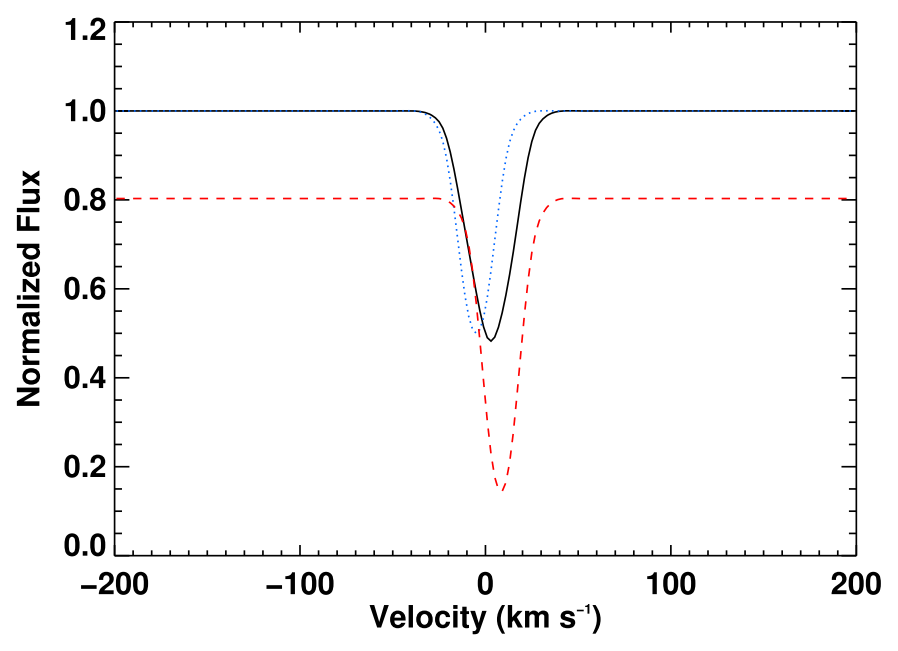


Figure 15. A sample model line profile generated using LSD profiles. The secondary star is shown with a red-dashed line, the primary is shown with a blue-dotted line, and the combined and renormalized model is shown with a solid black line.

primary are shallower than in the secondary), the value does not exactly match that necessary to fit the orbital model to the RV data. However, the synthesized spectra are computed without knowing the exact temperatures and gravities of the component stars. In addition, the final RV model used assumes a component flux ratio determined from the HST observation, which is from a very different epoch compared to all the RV measurements in Figure 6. As a result, this line depth ratio may not be exactly appropriate considering that the degree of spottedness on the component stars changes as the result of stellar rotation and likely has longer term changes with time.

# B.4. Comparison with Previous Studies and Mass Limits on a Possible Third Component

Rizzuto et al. (2020) performed a similar analysis on the same set of HST images of Hubble 4 that we presented in this paper. To account for the shutter-induced jitter in shorter exposures, they applied a Gaussian blur to the PSF used in both the A and B shutter positions, allowing both the extent and angle of the blur to vary in their fits. We apply a symmetric blur only in the B shutter position based on calibration data from Sabbi (2009). The flux ratio measurements are sensitive to the positions of the components relative to the size and orientation of the blur. Based on the size of the residuals (around  $\sim 5\%$  of the peak flux for both studies), our fits are of similar quality to those of Rizzuto et al. (2020).

Possibly as a result of the difference in the PSFs used, the flux ratios reported by Rizzuto et al. (2020) differ significantly from those reported in Table 4. The greatest difference is in F555W, where our measured flux ratio of  $0.801^{+0.082}_{-0.076}$  differs significantly from their measurement of  $0.402^{+0.083}_{-0.104}$ . Though the F555W measurement was omitted from their later analysis, in the five filters redder than 500 nm, the flux ratios reported here are consistently larger than those measured by Rizzuto et al. (2020). Rizzuto et al. (2020) also reported a greater-than-expected flux ratio of 0.65 measured in the NIR, as well as the presence of TiO lines in the unresolved spectrum of the binary.

The flatter spectral energy distribution (SED) ratio reported in Rizzuto et al. (2020) is best fit by spectra for the two components with similar temperatures, with the optimal fit finding  $T_{\rm eff}=4411\,\rm K$  for the primary and  $T_{\rm eff}=4254\,\rm K$  for the secondary. These temperatures are similar to the results of our unspotted model presented in Figure 14. However, as reported before, these temperatures do not match those expected for this system according to young star models (Baraffe et al. 2015). Although the best-fit spectra that assume no spot coverage match the NIR flux ratio of approximately 0.65, they do not predict the strong TiO features found in the unresolved spectrum of the binary.

To explain these observations, Rizzuto et al. (2020) proposed that the Hubble 4 system is in fact a hierarchical triple system. They suggested the "primary" of the resolved binary is in fact itself a close binary system in which  $T_{\rm eff}$  is  $\sim$ 4000 K for the more massive component. We use our RV measurements to place an upper limit on the mass of an unseen companion orbiting Hubble 4 A following the procedure described in Boyajian et al. (2016), which we summarize here. In this search we use the RV variations after subtracting the known binary contribution using the model described above in Appendix B.3 and also the fitted spot models described in Section 4.2. We phase fold the residual RVs to 10<sup>6</sup> periods, ranging from 2-1000 days. We then fit a sinusoid to each resulting RV curve via least squares to determine the RV amplitude and uncertainty,  $\sigma$ . We use the measured RV amplitudes and added  $2\sigma$  to get a conservative upper limit for the maximum allowed RV amplitude at each period.

To convert the RV amplitude to a companion mass, we assumed  $0.7\,M_\odot$  for the mass of the primary in Hubble 4 A, estimated by using the Baraffe et al. (2015) tracks and again assuming a system age of 2 Myr for a star with  $T_{\rm eff} = 4000\,{\rm K}$ . The mass limits are shown in Figure 16. Rizzuto et al. (2020) gave a maximum projected separation of  $\sim 0.5$  au. Inside this limit, we find  $M \sin i > 8\,M_{\rm Jup}$  exceeds our  $2\sigma$  detection limit. Galli et al. (2018) found the primary of the Hubble 4 system has a mass of  $\sim 1.2\,M_\odot$ . If this is in fact two stars with the more

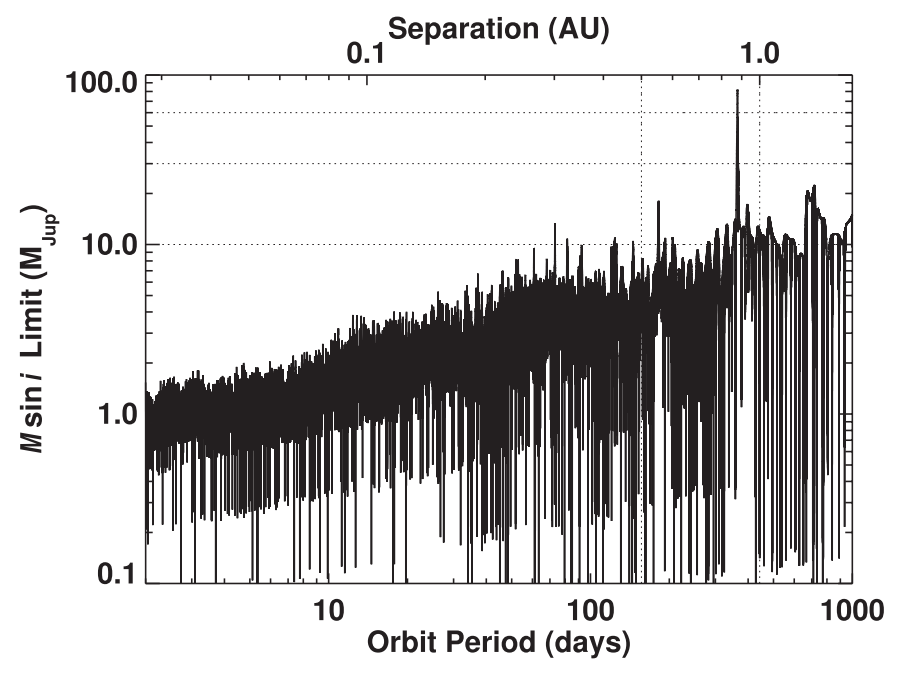


Figure 16. Mass limits on undetected companions around Hubble 4 A. Vertical-dotted lines at 0.5 and 1 au show orbital separations, and horizontal-dotted lines indicate companion masses of 10, 30, and  $60 M_{\text{Jup}}$ . The separations are computed for a test particle at the given orbit period.

massive having a mass of  $\sim 0.7 M_{\odot}$ , the third star in the system must have a mass of  $\sim 0.5 \, M_{\odot}$ . Combined with our  $8 \, M_{\rm Jup}$ companion mass limit, the orbit of such a companion would have to have an inclination of  $i \leq 0.92^{\circ}$ .

We also estimated the resulting SED ratios from the proposed triple system following the procedure described in Appendix B.1 and compared the results to the HST photometry. We used NextGen synthetic spectra and assumed the effective temperature of Hubble 4 B and the more massive component of Hubble 4 A are both 4000 K, and we assumed  $T_{\rm eff} = 3700$  K for the less massive component of Hubble 4 A. We also assumed the radii of the primary components are  $\sim 1.66$  and  $\sim 1.48 R_{\odot}$ , as given by Baraffe et al. (2015) isochrones, and we again assumed the radius of Hubble 4 B is  $1.7 R_{\odot}$ . The resulting model SED is much flatter than the SED measured from the HST photometry and is a worse fit than either of the fits shown in Figure 14. The predicted flux ratios are also much greater than those measured here or in Rizzuto et al. (2020), especially in wavelengths shorter than 500 nm.

Our RV measurements, combined with the Galli et al. (2018) orbit determination of the wide binary, place tight restrictions on the parameter space allowed for a third member of the Hubble 4 system. We also find that the optical SED ratios of the system measured from our analysis of the HST imaging of Hubble 4 does not match well the predicted flux ratios for the hierarchical triple system proposed by Rizzuto et al. (2020). While our analysis of the HST data differs from that of Rizzuto et al. (2020), their analysis of the HST data produces flux ratios inconsistent the hierarchical triple system they propose, particularly at shorter wavelengths. Our measured HST flux ratios, along with the NIR flux ratios given in Rizzuto et al. (2020), are more accurately reproduced by a model with large spot coverage on the  $T_{\rm eff} = 4530\,\rm K$  primary and an unspotted  $T_{\rm eff} = 4070\,\rm K$  secondary. The large spotted region on the primary could also be the source of the relatively strong TiO features observed in the spectra of the binary. Therefore, we have concluded that a model with highly spotted primary and a

relatively unspotted secondary, with no significantly contributing third companion, provides a more plausible explanation for the Hubble 4 system.

## **ORCID iDs**

Adolfo Carvalho https://orcid.org/0000-0002-9540-853X Christopher M. Johns-Krull https://orcid.org/0000-0002-8828-6386

L. Prato https://orcid.org/0000-0001-7998-226X Jay Anderson https://orcid.org/0000-0003-2861-3995

## References

Allard, F., Homeier, D., & Freytag, B. 2012, RSPTA, 370, 2765 Asplund, M., Grevesse, N., Sauval, A. J., & Scott, P. 2009, ARA&A, 47, 481 Baraffe, I., Homeier, D., Allard, F., & Chabrier, G. 2015, A&A, 577, A42 Bouvier, J., Cabrit, S., Fernandez, M., Martin, E. L., & Matthews, J. M. 1993, A&A, 272, 176

Boyajian, T. S., LaCourse, D. M., Rappaport, S. A., et al. 2016, MNRAS,

Bradshaw, S. J., & Hartigan, P. 2014, ApJ, 795, 79

Canfield, R. C., Penn, M. J., Wulser, J.-P., & Kiplinger, A. L. 1990, ApJ,

Cauley, P. W., Redfield, S., & Jensen, A. G. 2017, AJ, 153, 185

Chen, G., Casasayas-Barris, N., Pallé, E., et al. 2020, A&A, 635, A171

Chen, W., & Johns-Krull, C. M. 2013, ApJ, 776, 113

Choi, P. I., & Herbst, W. 1996, AJ, 111, 283

Czekala, I., Chiang, E., Andrews, S. M., et al. 2019, ApJ, 883, 22

Donati, J.-F., & Cameron, A. C. 1997, MNRAS, 291, 1

Donati, J.-F., Yu, L., Moutou, C., et al. 2017, MNRAS, 465, 3343

Doyle, L., Ramsay, G., Doyle, J. G., & Wu, K. 2019, MNRAS, 489, 437 Ehrenreich, D., Bourrier, V., Bonfils, X., et al. 2012, A&A, 547, A18

Fischer, D. A., Marcy, G. W., & Spronck, J. F. P. 2014, ApJS, 210, 5

Fisher, G. H., Canfield, R. C., & McClymont, A. N. 1985a, ApJ, 289, 434 Fisher, G. H., Canfield, R. C., & McClymont, A. N. 1985b, ApJ, 289, 425

Galli, P. A. B., Loinard, L., Ortiz-Léon, G. N., et al. 2018, ApJ, 859, 33 Gnevyshev, M. N. 1938, PGAOI, 27, 37

Gray, D. F. 2005, The Observation and Analysis of Stellar Photospheres (Cambridge: Cambridge Univ. Press)

Gullbring, E., Barwig, H., Chen, P. S., Gahm, G. F., & Bao, M. X. 1996, A&A, 307, 791

```
Hartig, G. F. 2008, Instrument Science Report, Space Telescope Science
  Institute, WFC3-2008-44
Hartmann, L., Hewett, R., Stahler, S., & Mathieu, R. D. 1986, ApJ, 309, 275
Hatzes, A. P. 1995, ApJ, 451, 784
Hauschildt, P. H., Allard, F., & Baron, E. 1999, ApJ, 512, 377
Hinkle, K. H., Joyce, R. R., Sharp, N., & Valenti, J. A. 2000, Proc. SPIE,
   4008, 720
Honda, S., Notsu, Y., Namekata, K., et al. 2018, PASJ, 70, 62
Horne, J. H., & Baliunas, S. L. 1986, ApJ, 302, 757
Houk, N., & Swift, C. 1999, Michigan Spectral Survey, Vol. 5
Huerta, M., Johns-Krull, C. M., Prato, L., Hartigan, P., & Jaffe, D. T. 2008,
    ApJ, 678, 472
Johns-Krull, C. M., & Herczeg, G. J. 2007, ApJ, 655, 345
Johns-Krull, C. M., Prato, L., McLane, J. N., et al. 2016, ApJ, 830, 15
Johns-Krull, C. M., Valenti, J. A., & Saar, S. H. 2004, ApJ, 617, 1204
Kalirai, J. S., MacKenty, J., Rajan, A., et al. 2009, Instrument Science Report,
   WFC3 2009-31
Kowalski, A. F. 2012, PhD thesis, Univ. Washington
Kowalski, A. F., Hawley, S. L., Wisniewski, J. P., et al. 2013, ApJS, 207, 15
Kraus, A. L., Ireland, M. J., Martinache, F., & Hillenbrand, L. A. 2011, ApJ,
   731, 8
Kurtovic, N. T., Pérez, L. M., Benisty, M., et al. 2018, ApJL, 869, L44
Mahmud, N. I., Crockett, C. J., Johns-Krull, C. M., et al. 2011, ApJ, 736, 123
Mann, A. W., Newton, E. R., Rizzuto, A. C., et al. 2016, AJ, 152, 61
Norton, A. J., Wheatley, P. J., West, R. G., et al. 2007, A&A, 467, 785
```

```
Osten, R. A., & Wolk, S. J. 2015, ApJ, 809, 79
Pecaut, M. J., & Mamajek, E. E. 2013, ApJS, 208, 9
Piskunov, N. E., Kupka, F., Ryabchikova, T. A., Weiss, W. W., &
  Jeffery, C. S. 1995, A&AS, 112, 525
Rice, J. B., Strassmeier, K. G., & Kopf, M. 2011, ApJ, 728, 69
Rizzuto, A. C., Dupuy, T. J., Ireland, M. J., & Kraus, A. L. 2020, ApJ,
  889, 175
Robertson, P., Stefansson, G., Mahadevan, S., et al. 2020, ApJ, 897, 125
Ryabchikova, T., Piskunov, N., Kurucz, R. L., et al. 2015, PhyS, 90, 054005
Saar, S. H., & Donahue, R. A. 1997, ApJ, 485, 319
Sabbi, E. 2009, WFC3 SMOV Program 11798: UVIS PSF Core Modulation,
  Technical Report ISR, WFC3-2009-20
Skinner, S. L. 1993, ApJ, 408, 660
Soderblom, D. R., Pendleton, J., & Pallavicini, R. 1989, AJ, 97, 539
Soto, M. G., & Jenkins, J. S. 2018, A&A, 615, A76
Stelzer, B., Fernàndez, M., Costa, V. M., et al. 2003, A&A, 411, 517
Tonry, J., & Davis, M. 1979, AJ, 84, 1511
Tull, R. G., MacQueen, P. J., Sneden, C., & Lambert, D. L. 1995, PASP,
  107, 251
Valenti, J. A. 1994, PhD thesis, Univ. California Berkeley
Valenti, J. A., & Fischer, D. A. 2005, ApJS, 159, 141
Vida, K., Leitzinger, M., Kriskovics, L., et al. 2019, A&A, 623, A49
Vidal-Madjar, A., des Etangs, A. L., Désert, J.-M., et al. 2003, Natur, 422, 143
Waldmeier, M. 1955, Ergebnisse und Probleme der Sonnenforschung (2nd ed.;
  Leipzig: Akad. Verlagsges)
```